Computational and Experimental Investigation of Li-doped Ionic Liquid Electrolytes: [pyr14][TFSI], [pyr13][FSI], and [EMIM][BF_4]

Justin B. Haskins,[†] William R. Bennett,[‡] James J. Wu,[‡] Dionne M. Hernández,[‡] Oleg Borodin,[¶] Joshua D. Monk,[†] Charles W. Bauschlicher, Jr.,[§] and John W. Lawson[*,‖]

ERC Inc., Thermal Protection Materials and Systems Branch, NASA Ames Research Center, Moffett Field, California 94035, USA, Electrochemistry Branch, NASA Glenn Research Center, Cleveland, OH 44135, USA, Electrochemistry Branch, Sensor & Electron Devices Directorate, U.S. Army Research Laboratory, Adelphi, Maryland 20783, USA, Entry Systems and Technology Division, NASA Ames Research Center, Moffett Field, California 94035, USA, and Thermal Protection Materials and Systems Branch, NASA Ames Research Center, Moffett Field, California 94035, USA

E-mail: john.w.lawson@nasa.gov

[*]To whom correspondence should be addressed

[†]ERC Inc., Thermal Protection Materials and Systems Branch, NASA Ames Research Center, Moffett Field, California 94035, USA

[‡]Electrochemistry Branch, NASA Glenn Research Center, Cleveland, OH 44135, USA

[¶]Electrochemistry Branch, Sensor & Electron Devices Directorate, U.S. Army Research Laboratory, Adelphi, Maryland 20783, USA

[§]Entry Systems and Technology Division, NASA Ames Research Center, Moffett Field, California 94035, USA

[‖]Thermal Protection Materials and Systems Branch, NASA Ames Research Center, Moffett Field, California 94035, USA

Abstract

We employ molecular dynamics (MD) simulation and experiment to investigate the structure, thermodynamics, and transport of *N*-methyl-*N*-butylpyrrolidinium bis(trifluoromethylsufonyl)imide ([pyr14][TFSI]), *N*-methyl-*N*-propylpyrrolidinium bis(fluorosufonyl)imide ([pyr13][FSI]), and 1-ethyl-3-methylimidazolium boron tetrafluoride ([EMIM][BF_4]), as a function of Li-salt mole fraction ($0.05 \leq x_{Li^+} \leq 0.33$) and temperature ($298\ K \leq T \leq 393\ K$). Structurally, Li^+ is shown to be solvated by three anion neighbors in [pyr14][TFSI] and four anion neighbors in both [pyr13][FSI] and [EMIM][BF_4], and at all levels of x_{Li^+} we find the presence of lithium aggregates. Pulsed field gradient spin-echo NMR measurements of diffusion and electrochemical impedance spectroscopy measurements of ionic conductivity are made for the neat ionic liquids as well as 0.5 molal solutions of Li-salt in the ionic liquids. Bulk ionic liquid properties (density, diffusion, viscosity, and ionic conductivity) are obtained with MD and show excellent agreement with experiment. While the diffusion exhibits a systematic decrease with increasing x_{Li^+}, the contribution of Li^+ to ionic conductivity increases until reaching a saturation doping level of $x_{Li^+} = 0.10$. Comparatively, the Li^+ conductivity of [pyr14][TFSI] is an order of magnitude lower than that of the other liquids, which range between 0.1-0.3 mS/cm. Our transport results also demonstrate the necessity of long MD simulation runs ($\sim$ 200 ns) required to converge transport properties at room T. The differences in Li^+ transport are reflected in the residence times of Li^+ with the anions ($\tau^{Li/-}$), which are revealed to be much larger for [pyr14][TFSI] (up to 100 ns at the highest doping levels) than in either [EMIM][BF_4] or [pyr13][FSI]. Finally, to comment on the relative kinetics of Li^+ transport in each liquid, we find that while the net motion of Li^+ with its solvation shell (vehicular) significantly contributes to net diffusion in all liquids, the importance of transport through anion exchange (hopping) increases at high x_{Li^+} and in liquids with large anions.

Introduction

Over the past decade, there has been extensive research concerning the development of rechargeable secondary batteries with high energy density.[1,2] Currently, lithium ion batteries with organic electrolytes represent the state of the art, though electrolyte stability and a maximum energy density of around 200 W·h/kg remain limiting factors.[3] A potential advancement beyond current lithium ion technology is the use of lithium metal anodes, which would ideally lead to a 5-fold gain in energy density. However, against these anodes, conventional organic electrolytes are unstable and lead to both poor cyclability and potentially hazardous lithium dendrite formation.[4] As an alternative, room temperature ionic liquids, which have low volatility, large electrochemical windows, and the ability to solvate Li-salts, have been shown to form stable solid-electrolyte interfaces (SEI) against lithium metal, concurrently allowing improved cycling and suppression of problematic dendrites.[5–13] In this regard, the most promising ionic liquids generally contain either the bis(trifluoromethanesufonyl)imide ([TFSI]) anion or the bis(fluorosufonyl)imide ([FSI]) anion, both of which have been shown to allow stable cycling with lithium metal anodes.[5–12] Comparatively, the stability of [TFSI] is superior to [FSI],[11,14] while the discharge rate of [FSI], $\sim$10 mA/cm^2,[10,11] has been reported to be larger than [TFSI], 1-1.75 mA/cm^2.[9,12,15] High discharge rates and reasonable stability can also be obtained with mixtures of ionic liquids having small anions, notably boron tetrafluoride ([BF_4]),[12,13,16] with organic additives such as vinylene carbonate (VC), though cycling in such cases may be generally limited.[12,16]

Bulk transport properties, including viscosity, diffusion, and ionic conductivity, of the ionic liquids are important for electrochemical performance, with low viscosity and high diffusion being key to high discharge rates. However, while the transport properties of neat ionic liquids have been characterized in detail,[17–22] mixtures of ionic liquids with Li-salts have not been as thoroughly investigated, with most studies measuring properties at select values of x_{Li^+}.[5,6,9,13,14,21] Indeed, due to the many possible x_{Li^+} and T conditions, providing a complete characterization of the influence of Li-salt is difficult, and only a few

liquids have been studied comprehensively in this manner.[23–25] Notably, extensive pulsed-field-gradient spin-echo NMR studies reported in the works of Hayamizu *et al.*[24] and Nicotera *et al.*[25] for 1-ethyl-3-methylimidazolium ([EMIM]) [BF_4] doped with Li[BF_4] and N-methyl-N-propylpyrrolidinium ([pyr13]) [TFSI] doped with Li[TFSI], respectively, have mapped the diffusion and transference numbers as a function of x_{Li^+}.

Complementary to bulk property measurements, the solvation environment of Li^+ can provide important insights into a given liquid. As an example, high energy X-ray diffraction (HEXRD) can be used to obtain the liquid structure factor, which in combination with molecular dynamics (MD) simulation is an effective tool for finding intermolecular distances. HEXRD measurements have been performed to find the relative intermolecular separations for ionic liquids with the [TFSI] and [FSI] anions[26–28] and have, interestingly, been adapted to characterize Li clusters.[28] Finer structural aspects, such as the binding configurations in the Li^+ solvation shell, are more difficult to obtain and generally require IR or Raman measurements in combination with density functional theory (DFT) computations.[27,29–32] Such procedures have been successfully applied, again, to [TFSI] and [FSI] to identify the conformational equilibrium between their cis and trans rotamers[29–31] as well as to determine their solvation numbers and preferential bonding states with Li^+,[27,32] which include one-fold (monodentate) and two-fold binding (bidentate).

As a supplement to experimental characterization, MD is an effective tool to evaluate many fundamental structural, thermodynamic, and transport properties while allowing an atom-level view of the structure. Various force fields have been recently parameterized for the explicit purpose of ionic liquid simulation, and many of these have matured to the point of producing experimentally quantitative thermodynamic properties.[33–37] In particular, polarizable force fields, where each atom is given an environment-dependent atomic dipole, stand out as systematically providing superior transport properties in neat ionic liquids.[34,38,39] More recently, ionic liquid force fields have been adapted to treat the important case of mixtures with Li-salts.[40–43] These force fields have been primarily applied to a range of sys-

tems, including Li[TFSI] in liquids with pyrrolidinium or imidazolium cations and [TFSI] anions,[41,42,44,45] Li[FSI] in [pyr14][FSI],[45] Li[BF_4] in liquids with imidazolium cations and [BF_4] anions,[43] and Li[PF_6] in [EMIM][PF_6].[46] Such studies generally focus on structure at low x_{Li^+}, where clustering is not influential, and on properties at high-T, where the typically glassy ionic liquid dynamics become amenable to MD simulation. Polarizable models, as in the case of neat ionic liquids, are expected to provide more accurate results for both thermodynamics and transport properties for systems with Li salt additions.[41,44,45]

In the present study, we employ both theoretical and experimental methods to investigate the influence of Li-salt doping on the properties of three potential ionic liquid electrolytes. The three ionic liquids of interest (see Fig. 1) are N-methyl-N-butylpyrrolidinium bis(trifluoromethylsufonyl)imide, N-methyl-N-propylpyrrolidinium bis(fluorosufonyl)imide, and 1-ethyl-3-methylimidazolium boron tetrafluoride, denoted as [pyr14][TFSI], [pyr13][FSI], and [EMIM][BF_4], respectively. These ionic liquids have been selected primarily because of their stability against Li-metal anodes.[8,9,12] However, their high ionic conductivity and low viscosity[21,22,24] make them promising electrolytes for conventional lithium ion batteries[5,14,47] as well.

Theoretically, we perform a comprehensive set of polarizable MD simulations, using the Atomistic Polarizable Potential for Liquids, Electrolytes, & Polymers (APPLE&P),[33,34,40] to investigate the influence of temperature and lithium doping on the structure, thermodynamics, and transport properties of these liquids. Li-salt is introduced into each ionic liquid using the host anion (*i.e* [pyr14][TFSI] would have the Li[TFSI] salt), and we probe the influence of Li-salt doping from small molar fractions (0.05) to the glassy upper limit of liquid stability ($\sim$0.33). Importantly, we analyze the ionic liquid properties from room temperature up to 120 °C at all levels of Li-doping, and, in this regard, our study requires very long simulation times ($\sim$200 ns) to accurately determine the transport coefficients in low-T ionic liquids.

In addition, we have performed a number of room temperature experiments on both the neat ionic liquids and 0.5 molal solutions of Li-salt in the ionic liquids. Our experiments

include measures of density, pulsed field gradient spin-echo NMR measurements of diffusion coefficients, and electrochemical impedance spectroscopy measurements of ionic conductivity.

Methods

APPLE&P Interatomic Potential

To accurately describe the complex, environment-dependent electrostatic interactions of ionic liquids with MD simulation, we employ the APPLE&P force field as parameterized by Borodin and coworkers.[33,34,40] The energy in APPLE&P is decomposed into intramolecular, repulsive-dispersive, and electrostatic terms. The intramolecular interactions consist of harmonic bonds, angles, and improper dihedrals, while torsional dihedrals are represented by an order-N harmonic series. The repulsive-dispersive interactions are treated with a modified form of the exponential-6 Buckingham potential, which includes a correction term to account for close atomic approaches, given by

$$U^{rd}(r_{ij}) = A_{ij}e^{-B_{ij}r_{ij}} - C_{ij}r_{ij}^{-6} + D_{ij}\left(\frac{12}{r_{ij}}\right)^{12}. \tag{1}$$

Furthermore, each atom is assigned a static parital point charge, all of which mutually interact through Coulomb's law. While many of these interaction terms are standard to MD simulation, the unique aspect of APPLE&P that allows for a high-fidelity representation of ionic liquid energetics is the inclusion of self-consistent atomic polarization. This is achieved by associating an atomic polarizability (α) to each atom, which defines the atomic dipole moment as proportional to the local electric field, $\boldsymbol{\mu}_i = \alpha\mathbf{E}(\mathbf{r}_i)$. Self-consistency is then achieved by updating the electric field with the evolved dipole contributions and recalculating the atomic dipole moment until changes in polarization energy, given by

$$U^{pol}(r_i) = -\frac{1}{2}\boldsymbol{\mu}_i \cdot \mathbf{E}^0(\mathbf{r}_i), \tag{2}$$

where $\mathbf{E}^0(\mathbf{r}_i)$ is the electrostatic field contribution from permanent charges only, reach a requisite tolerance. Specific to the [FSI] and [TFSI] anions investigated in this work and in addition to the atom center terms, a single lone-pair force center is associated with the S-N-S bridge, and the position of this center is instantaneously determined during the simulations as a given distance, $\ell = 1.4$ Å, along a bisector of the S-N-S angle.

Molecular Dynamics Simulations

The majority of the MD simulations in the present work are performed with the Large-scale Atomic / Molecular Massively Parallel Simulator (LAMMPS).[48] We have modified LAMMPS to include the following functionalities required by APPLE&P: lone pairs force centers for the [TFSI] and [FSI] anions; self-consistent update of atomic dipoles using the previously discussed atomic polarizability; and energy, force, and virial terms that arise from long range charge-dipole interactions. For purposes of validation and statistical error estimation, a small subset of simulations on [pyr14][TFSI] are duplicated with *Lucretius*[49] an simulation package specifically tailored to perform MD simulation using the APPLE&P. The simulations are integrated using a 3-2-1 reversible reference system propagation algorithm (rRESPA),[50] which allows the use of a large 3 fs timestep for the long-range Ewald summation of the charge and dipole interactions; a 1.5 fs timestep for local charge, repulsive-dispersive, and dihedral interactions; and 0.5 fs for the remaining bonds, angles, and improper dihedrals. The cutoff used for non-bonded interactions is 12 Å for [pyr14][TFSI] and [pyr13][FSI] systems and 11 Å for [EMIM][BF_4] systems; the cutoff used for non-bonded interactions in the 1.5 fs rRESPA step is 7 Å. For further efficiency, a coupled reaction field/Ewald summation formalism is employed in the outer rRESPA partition to evaluate the dipole-dipole (reaction field) and dipole-charge (Ewald summation) long range interactions; these computations are performed iteratively in the outer partition until the change in the dipole energy reaches a convergence criterion of 10^{-9} kcal/mol.

The systems used in our MD simulations contain 144 cation/anion pairs for the [pyr14]-

[TFSI] ionic liquid and 216 pairs for both the [pyr13][FSI] and [EMIM][BF_4] ionic liquids, and Li-salt is introduced into each system by replacing a given number of cations with lithium ions. At $T = 298$ K, we perform MD simulations across a range of Li-salt mole fractions (x_{Li^+} from 0.05 to 0.33), while at higher-T we perform calculations at select values of x_{Li^+} that correspond to specific experimental conditions. To equilibrate each system, we perform simulations at ambient P and the desired T using the Nosé-Hoover thermostat and barostat. The thermalization is carried out over 20 ns at each T, which we have found to be sufficient for density convergence in the system with the lowest temperature and the highest Li-salt doping.

There are additional challenges to the MD simulation of ionic liquids with Li-salt doping, primarily due to the glassy nature of the systems at $T \leq 333$ K. This is especially relevant when considering the calculation of transport coefficients, which are well known to converge more slowly than other properties like density. To ensure convergence, we progressively compute the transport properties by incrementally adding 30-50 ns of simulation statistics to the transport average until the change in the property of interest is less than 5%. In this way, we have determined that simulations of 200 ns are required to converge the transport properties for the $T = 298$ K and 333 K systems, while 90-120 ns simulation times appear more than sufficient to converge properties at higher T.

Experimental Techniques

We have performed extensive experimental characterization of [pyr14][TFSI], [EMIM][BF_4], and [pyr13][FSI] in both neat samples and those having 0.5 moles of Li-salt per kilogram of ionic liquid, denoted as a 0.5 molal solution (m). For these liquids we have measured the density, diffusion and ionic conductivity.

Density is measured under an argon atmosphere (humidity $\leq$ 1 ppm) in a glovebox at room temperature, using a 5 cm^3 graduated cylinder (0.1 cm^3 graduations). Mass is measured to the nearest milligram with a calculated uncertainty of <3%.

The diffusion coefficients of cation and anion species are measured by pulse-field gradient spin echo NMR. The signals of the methyl ^{1}H and ^{19}F are used to determine the self-diffusion coefficients (D^+ and D^-) of the cations and anions, respectively, and in the presence of lithium salt, the signal of ^{7}Li is used to determine the Li^+ diffusion coefficient. In the NMR experiments, D is obtained using

$$ln(A/A_0) = -D\gamma^2(\nabla - \delta/3)\delta^2 g^2, \tag{3}$$

where A and A_0 represent the signal integrals in the presence of and absence of the pulsed-field gradient, γ is the nuclear magnetogyric ratio, ∇ is the time interval between the two gradient pulses, δ is the gradient pulse width, and g is the gradient magnitude.

Samples are loaded into a 5 mm cylindrical thin wall 9" NMR tube inside a glovebox and at room temperature, and then the NMR tube was sealed tightly with the cup coming with the tube as the tube was purchased. A total of four samples were prepared and loaded into the tubes for NMR measurements: [pyr14][TFSI]; 0.5 m Li[TFSI] in [pyr14][TFSI]; [EMIM][BF_4]; 0.5 m Li[BF_4] in [EMIM][BF_4]. All samples were made with pure materials and no d-solvent was added. Although the samples inside the NMR tubes were cupped and tightly sealed, the samples were also kept in a desiccator to prevent moisture pick-up before measurement.

The samples are inserted into 5 mm BB (broad band) PFG (pulsed field gradient) probe equipped with a triple axis gradient amplifier, and all the measurements were collected on a Varian VNMRS 500 MHz spectrometer. The grade type "ppp" was used to achieve the highest gradient strength of 130 G/cm, which is the result of using two PFG amplifiers together with the grade type selection. A doped D_2O standard sample from Agilent was used to calibrate the gradients before the experiments are carried out. In addition, before each experiment, the 90° pulse width was determined on each nuclei (^{1}H, ^{19}F, and ^{7}Li) for every sample. Typically, 32-64 transients were used to collect the data for each experiment

depending on the signal to noise ratio. The diffusion coefficients of Li^+, cations, and anions are measured at 30°C, with sample temperature being controlled by a variable temperature control unit using a heated dry air. The experimental errors in the diffusion coefficient measurements are estimated to be less than 3%.

Ionic conductivities are determined by electrochemical impedance spectroscopy (EIS) methods, using a Solarton 1250 frequency response analyzer coupled to a Solartron 1286 electrochemical interface. The operation of these instruments is automated using Scribner and Associates' Zpolt® software for Windows. Impedance is measured using a 10 mV amplitude signal (55 kHz to 0.1 Hz) with the cell held at the open-circuit potential. Such methods have been previously used to measure the conductivity of polymer electrolytes.[51,52] The conductivity fixture, displayed in Figure S6 of the supplementary, uses 1-inch diameter, AISI 304 stainless steel electrodes, mounted in rigid, electrically insulating plates. The electrodes are lapped flat with the inside face of the insulating plate, and polished with 600 grit emery cloth. Steel dowel pins control the alignment of the electrodes, and inter-electrode spacing is established by a slotted, polypropylene mask, which confines the liquid sample between the electrodes. The electrode spacing is typically 1 mm.

Material handling and cell assembly are performed inside an inert atmosphere glovebox to minimize the absorption of water (humidity $\leq$ 1 ppm). After assembly, the fixtures are sealed in modified Nalgene^{TM} jars before being transferred out of the glovebox atmosphere for testing. Measurements are typically completed between 20^oC and 80^oC, with temperature being allowed to stabilize at $\pm 0.1^o$C before testing. Electrode spacing, L, and area, A, are controlled by the fixture, and electrochemical impedance data provides a measure of sample bulk-resistence, R_b. Ionic conductivity, λ, is calculated using $\lambda = L/AR_b$. The error in the calculated conductivity is $\pm 10\%$, based on tolerances for L, A, and R_b.

Structural Implications of Li-doping

Ionic Liquid Coordination and Conformations

To assess the influence of Li-salt on the molecular coordination of the ionic liquid, we compute the center of mass radial distribution function, g(r), between the cations and anions, Fig. 2. Interestingly, increased Li-salt doping induces only subtle changes in the cation-cation distributions, $g^{++}(r)$, and cation-anion distributions, $g^{+-}(r)$, with the relative magnitude of the first solvation shell slightly shifting downward. Alternatively, the first solvation shell of the anion-anion distributions, $g^{--}(r)$, exhibits a significant split into two individual peaks, which occurs such that there is a well defined peak at small r and a more diffuse peak at larger r. The former of these peaks represents the closely neighbored anions that are strongly bound to Li^+, with average neighbor distances of 6.5 Å, 6 Å, and 5 Å for [TFSI], [FSI], and [BF_4], respectively. The latter peak, which is situated at 12 Å, 10 Å, and 9 Å for [TFSI], [FSI], and [BF_4], respectively, represents the remaining anions coordinated to cations and suggests that the average anion-anion neighbor distance around each ionic liquid cation increases with Li-salt doping.

To further elaborate on the coordination of the ions, we compute the average number of anions neighboring each cation, given by $n^{\text{cation}}(\text{anion}) = 4\pi\rho \int g^{+-}(r) r^2 dr$, where ρ is the number density of anions and the integral is taken over the first solvation shell. Of the neat liquids, cations in [pyr14][TFSI] have the fewest coordinated anions, $n^{[\text{pyr14}]}([\text{TFSI}]) = 5.6$, followed by [EMIM][$BF_4$] with $n^{[\text{EMIM}]}([BF_4]) = 6.7$ and [pyr13][FSI] with $n^{[\text{pyr13}]}([\text{FSI}]) = 7$. While $g^{+-}(r)$ apparently changes little with increased Li-salt, $n^{\text{cation}}(\text{anion})$, Fig. 3a, shows a pronounced increase, with each cation having on average more than one additional coordinating anion at the highest lithium mole fraction, $x_{Li^+} = 0.33$. This qualitatively agrees with the noted splitting behavior of the first solvation shell of $g^{--}(r)$, as more anion neighbors would have increased mutual electrostatic repulsion that would shift their coordinating distance to larger r. Of equal importance, this also implies that Li^+, on average, maintains

fewer neighboring anions than that of an ionic liquid cation, and this duality between cations with a large, unfavorable number of anions neighbors and Li^+ with fewer, strongly bound anions could be an energetic penalty to Li-solubility at high levels of doping.

An additional point of interest is the fact that the larger anions, [TFSI] and [FSI], assume distinct cis and trans rotamers that can be markers for changes in binding preference brought about by Li-salt doping. In the ionic liquids, we have mapped out the distributions of the C-S$\cdots$S-C and F-S$\cdots$S-F dihedrals, ϕ, for [TFSI] and [FSI], respectively, noting that cis conformations occur when ϕ approaches zero and trans conformations occur at ϕ close to 180°; the native distributions at room temperature are mapped out in Fig. S1 of the supplemental material.[53] It appears that the conformational distribution of cis and trans anions are slightly influenced by Li-salt levels, shown in Fig. 3b, which presents the conformational distribution at $T = 298$ K as a function of x_{Li^+}. While cis-[TFSI] is slightly more probable (54 %) and cis-[FSI] is slightly less probable (36 %) than trans conformations at $x_{Li^+} = 0$, the population of cis rotamers increases with increasing Li-salt doping. This agrees with various coupled Raman/DFT investigations of these anions, showing that cis and trans conformers of [FSI][26,54] and [TFSI][29,31] exist in equilibrium in liquid phases, with the population of cis increasing with Li-salt doping.[30]

Li^+ Solvation Shell

As the most general measure of the lithium solvation structure, we compute g(r) between Li^+ and the center of mass of the ionic liquid anions as well as Li^+ and the atomic species that mediate binding with the anion, which is O for [(T)FSI] and F for [BF_4]. As shown in Fig. 4a-c, [TFSI] and [FSI] show split initial peaks centered around 4 Å, while [BF_4] has a single narrow peak around 3 Å that changes little with increasing lithiation. The split first solvation shell of [TFSI] and [FSI] is primarily an isomeric effect, which leads to cis-[(T)FSI] having a closer center of mass distance to bound Li^+ than trans rotamers; however, the variation in the relative heights of the peaks with x_{Li^+} also signify changes in Li^+/anion

bonding configuration that will be discussed more fully later. The corresponding atomic g(r) reveal lithium/atom binding distances close to 2 Å, Fig. 4d-e, and further show no net change in structure with increasing x_{Li^+}, though the heights of the solvation shells shift slightly downward. The slight changes in g(r) are again more prominent when considering the total number of neighbors, Table 1. As previously speculated, Li^+ maintains far fewer neighbors than ionic liquid cations, with n^{Li^+}(anion) being less than four in [pyr14][TFSI] and four or greater for [pyr13][FSI] and [EMIM][BF_4]. Increasing the lithium-doping levels generally increases the number of relative anion neighbors, with the strongest effect being seen in [pyr14][TFSI] and [pyr13][FSI], while the atomic coordination number is generally maintained, or barely increasing as with [FSI]. This of course implies that the number of Li^+ bonds per anion decreases at higher x_{Li^+}.

Expanding on this, we have identified the preferential binding states of Li^+ with the ionic liquid anions, representative structures and binding distances of which are given in Fig. S2.[53] For each of our systems, we find states in the bulk liquid that correspond to Li^+ having a single bond with each anion, or a monodentate configuration (κ^1), as well as those having a two-fold bond with each anion, or a bidentate configuration (κ^2). The binding distances increase in magnitude with $Li^+ - O^{[FSI]} > Li^+ - O^{[TFSI]} > Li^+ - F^{[BF]_4}$, and, consequently, this is reflected in the binding energetics, which follow Li^+-[FSI] < Li^+-[TFSI] < Li^+-[BF_4]. A more detailed look at the binding energetics reveals κ^2 binding is generally stronger than κ^1 states, which are not stable in the gas phase for [TFSI] and [FSI], though solvation effects in MD simulations apparently stabilize κ^1 in [TFSI] and [FSI] with respect to gas phase. The extent of the stabilization of κ^1 can be seen through comparison of the relative proportion of κ^1 binding to κ^2 binding, Fig. 5, which reveals that only [TFSI] has appreciable quantities of κ^2 binding (38%) at low x_{Li^+}, while [BF_4] and [FSI] have 95% and 96% κ^1 binding, respectively. Increasing lithium concentration further increases the proportion of κ^1 to κ^2 in all cases, though this effect is strongest in [TFSI] with a 30% increase in κ^1 binding at $x_{Li^+} = 0.33$.

As a final note on the lithium solvation shell, we depict in Fig. 6 the most likely coordination complexes of Li^+ with neighboring anions as found at $T = 298$ K and $x_{Li^+} = 0.05$, where the influence of Li^+ aggregates is minimal as shown in the Li^+ - Li^+ radial distribution functions in Fig. 7. In [pyr14][TFSI], roughly 66% of the Li^+ is coordinated by two κ^1 anions and one κ^2 anion, though complexes having two κ^2 anions with one κ^1 anion (18%) and four anions that are exclusively κ^1 (12 %) are also competitive. In the other liquids, Li^+ is almost predominantly coordinated by four κ^1 anions, with 80% and 83% of Li^+ assuming this coordination in [pyr13][FSI] and [EMIM][BF_4], respectively. The remaining coordination complexes in these two liquids are generally composed of one κ^2 anion and three κ^1 anions, which leads to Li^+ being atomically 5-coordinated. The T-dependence of the coordination complexes is weak, though monodentate configurations become marginally more favorable at high-T; a full analysis of the likelihood of a given coordination complex found in our systems as a function of T is further illustrated in Fig. S3.[53]

Qualitatively, the solvation structures presented here agree with available MD simulations of similar systems that use both polarizable and non-polarizable force fields.[42,44,45,55] When compared to experiment at higher x_{Li^+}, however, our predicted lithium solvation structures for [pyr14][TFSI] and [pyr13][FSI] have higher anion coordination numbers. Infrared and Raman spectroscopy coupled with DFT for Li[TFSI] and Li[FSI] in imidazolium-based ionic liquids[27,32] have been interpreted as showing that [TFSI] prefers two coordination while [FSI] prefers three coordination. The experimentally reported coordination numbers are evaluated in systems having $x_{Li^+} > 0.05$, which, as shown in the following section, form significant quantities of Li^+ aggregates. It is well known that such aggregates have the net effect of reducing the Li^+/anion coordination number,[32] and, as it is not simple to spectroscopically characterize their contribution to the total measure of coordination, could be the primary reason for the discrepancy between our coordination number and that of experiment.

Li^+ Clusters

As previously mentioned, spectroscopic experiments[32] have noted that the Li^+/[TFSI] coordination number decreases at high x_{Li^+}, which has been attributed to the tendency of Li^+ to aggregate into clusters - networks of lithium ions bound by shared, or bridging, anions. The signature of such clusters has additionally been noted in HEXRD experiments[28] as well as MD simulations.[41] Here, too, we observe the presence of Li^+ clusters and attribute the majority of the aforementioned x_{Li^+}-mediated structure dependence to their formation. To put the magnitude of this effect into perspective, we first look at the probability of finding a cluster with a given number of bridged Li^+ ions, N_{Li^+}, as a function of x_{Li^+}, shown in Fig. 8. In all cases, as x_{Li^+} increases, the average cluster size increases, with the probability of finding a Li^+ not associated with a cluster decreasing from ∼80-90% at $x_{Li^+} = 0.10$ to $\sim 50\%$ at $x_{Li^+} = 0.33$. There also appears to be a correlation between anion size and cluster size, with larger anion sizes leading to progressively fewer, and smaller, clusters. At high doping levels the largest clusters observed in our systems are $N_{Li^+} = 5$ in [pyr14][TFSI] and $N_{Li^+} = 6$ in [pyr13][FSI] and [EMIM][BF_4].

It is further instructive to consider the radial distribution function of Li^+ with Li^+, which are displayed in Fig. 7 for multiple values of x_{Li^+}. Of primary importance are the well-defined peaks in the initial $r < 10$ Å region that signify Li^+ aggregation. From inspection of simulation trajectories, peaks between ∼5-10 Å represent lithium ions in small clusters, where possible anion binding sites are not saturated and allow configurational entropy to maximize Li^+ separation. As larger clusters form, internal anions become more highly networked until all possible binding sites, including those imposing small Li^+ separations, are saturated, which is represented by the peaks in the 4-5 Å regions. The initial peak is not present in [pyr14][TFSI] with $x_{Li^+} = 0.05$, suggesting no large clusters have formed, while the peak is present in both [pyr13][FSI] and [EMIM][BF_4]. In all cases, the relative height of the first peak to the second peak increases with x_{Li^+} and indicates the formation of large clusters.

As previously illustrated in Figs. 3a and 5, [TFSI] and [FSI] tend toward κ^1 binding and

cis-rotamers as lithium-salt doping increases. To examine the contribution of Li^+ aggregation to these changes, we have evaluated the probability of finding the cis rotamer and κ^1 binding in anions coordinated with multiple Li^+, the $N_{Li^+} = 5$ cluster represented in Fig. 9 showing the possible anion coordinations (one Li^+ being the minimum and four Li^+ being the maximum). For both the [TFSI] and [FSI] anions, as coordination increases, we find that the anions tend to primarily assume κ^1 binding states and cis configurations. At the highest coordination, both anions are 100% κ^1, each available O binding to a Li^+, while 86% of [TFSI] anions and 82% or [FSI] anions assume the cis conformation. These changes mirror experimental studies of the condensed phases of Li[FSI] and Li[TFSI], which also generally trend toward monodentate binding[56] and cis-rotamers.[57,58] Further evidence of the influence of clusters is provided in Figs. S4 and S5 of the supplementary, which explicitly evaluate the cluster contributions to changes in cis-rotamers and κ^1 binding in the same manner as Figs. 3a and 5.

Thermodynamic and Transport Properties

Density

The density (ρ) of our ionic liquid systems is shown in Fig. 10 for both the neat systems as well as those doped with Li-salt. We find that density agrees to within 1% of experimental measures for both the neat and Li-salt doped liquids. Furthermore, the densities of the neat ionic liquids show the typical linear decrease with rising T. We find that ρ trends upward with the size of the ionic species, with $\rho^{[\mathrm{pyr14}][\mathrm{TFSI}]} > \rho^{[\mathrm{pyr13}][\mathrm{FSI}]} > \rho^{[\mathrm{EMIM}][\mathrm{BF_4}]}$, which is sensible in light of the fact that average ion separations, on the basis of the g(r) results in Fig. 2, do not appreciably change from one liquid to another. The introduction of Li-salt, Fig. 10b, results in a near-linear increase up to the highest doping levels investigated, $x_{Li^+} = 0.33$. Of the three liquids [pyr13][FSI] shows the least linearity and, correspondingly, the largest ρ response to Li-salt doping, with $\rho^{[\mathrm{pyr13}][\mathrm{FSI}]}$ approaching that of [pyr14][TFSI]

at high x_{Li^+}. The relatively large ρ increase is indicative of the efficient packing of [FSI] around [pyr13] and Li^+, which is supported on the basis of Fig. 3a and Table 1, where the [pyr13][FSI] have the largest values of n^{cation}(anion) and n^{Li^+}(anion) at high x_{Li^+}.

Transport Properties

To compute the shear viscosity (η_{xy}) of the ionic liquids, we have employed the Green-Kubo relation,

$$\eta_{xy} = \frac{V}{k_B T} \int_0^\infty \langle P_{xy}(t) P_{xy}(0) \rangle \, dt, \tag{4}$$

where V is system volume, k_B is Boltzmann's constant, and P_{xy} is shear stress. The viscosity of [pyr14][TFSI], [EMIM][BF_4], and [pyr13][FSI] is shown in Fig. 11 for both the neat liquids and those having $x_{Li^+} = 0.10$ over the T range 298 K to 393 K. All of our computational estimates show agreement to within 20% of available experimental measures.[19,24,45] Additionally, η_{xy} exhibits both a rapid decrease as T increases and a significant increase with x_{Li^+}. At low-T, [pyr14][TFSI] has the largest values of η_{xy}, which is slightly less than a factor of two greater than that [EMIM][BF_4] and [pyr13][FSI], which has the lowest η_{xy}. At high-T, η_{xy} of all systems are comparable, though, interestingly, at this point Li-salt doping has less influence on η_{xy} of [pyr14][TFSI] and [pyr13][FSI] than that of [EMIM][BF_4].

We compute diffusion coefficients with the Einstein relation,

$$\mathrm{D}^\beta = \lim_{t \to \infty} \frac{1}{6 \mathrm{n}^\beta} \frac{d}{dt} \left\langle \sum_{i=1}^{n^\beta} |\mathbf{r}_i(t) - \mathbf{r}_i(0)|^2 \right\rangle, \tag{5}$$

where the diffusion coefficient, D, for molecular species β is estimated using the position, $\mathbf{r}$, of each of the n^β atoms belonging to species β. In all of our quoted values of D, we have applied a hydrodynamic correction, which accounts for the influence of the finite simulation cell on the diffusion coefficient. The correction, D^{FSC}, is calculated according to

$$\mathrm{D}^{\mathrm{FSC}} = \frac{2.837 k_B T}{6 \pi \eta L}, \tag{6}$$

with L being the average MD simulation cell length. Measures for the diffusion coefficients of [pyr14][TFSI], [EMIM][BF_4], and [pyr13][FSI], both neat and with $x_{Li^+} = 0.10$, are given in Fig. 12 for the the T range 298 K to 393 K. Our computational values of D for the neat ionic liquid cations and anions in [EMIM][BF_4] match available PFG-NMR measures to within 5-15%,[24,45] while variations in experimental measures of D in neat [pyr14][TFSI] lead to broad range of potential error (5-50 %).[19,21,45] In general, our estimates of Li^+ diffusion are also within this error tolerance as well; however, we note that at high-T, D of Li^+ in the [pyr14][TFSI] system seems to be underestimated by a factor of ∼2-3, with different experiments showing large variations and predicting the Li^+ diffusion to rapidly approach that of [TFSI] at $T > 333$ K. For [pyr14][TFSI], Fig. 12a and b, Li-salt doping reduces the diffusion coefficients of all molecular species, with the general relative magnitudes of diffusion following $D^{Li^+} < D^{[TFSI]^-} < D^{[pyr14]^+}$. The same general trends apply to [EMIM][BF_4], Fig. 12c and d, as well as [pyr13][FSI], Fig. 12e and f, and the relative magnitudes of diffusion follow [EMIM][BF_4] > [pyr13][FSI] > [pyr14][TFSI]. Interestingly, in contrast to the other liquids, the cations in [pyr13][FSI] tend to have a lower diffusion than the anions.

We compute ionic conduction (λ) using an expression akin to the Einstein relation for D,

$$\lambda = \lim_{t\to\infty} \frac{e^2}{6Vk_BT} \left\langle \left| \sum_i^{all} [q_i \mathbf{r}_i(t) - q_i \mathbf{r}_i(0)] \right|^2 \right\rangle, \tag{7}$$

where e is the elementary unit of charge and the sum is taken over all atoms. For [pyr14][TFSI] and [EMIM][BF_4], Fig. 13 a and b, our computed λ generally shows agreement to within 15% of experiment,[19,24,53] with the major exception being $T = 298$ K, where the λ of [pyr14][TFSI] is a lower bound with an error ∼40%. For [pyr13][FSI], Fig. 13 c, on the other hand, there is considerable scatter in the experimental data, our computed values agreeing to within 10% of the lowest estimates and to within 30% of the highest estimates. The significant scatter in [pyr13][FSI] λ measurements has been previously noted by Zhou and coworkers,[22] who suggest moisture contamination as a possible cause of higher values of λ. Additionally, for Li-salt

doped systems, underestimates of λ could be a repercussion of the slight overbidding of the force field for [TFSI] and [FSI] to Li^+ when compared to quantum chemical computations.[59] As expected, T has a strong influence on λ, which increases by an order of magnitude from 298 K to 393 K, and the addition of Li-salt decreases the net ionic conduction. At high-T, the ionic conduction of [EMIM][BF_4] is a factor $\sim$4 greater than [pyr14][TFS] and a factor of $\sim$ 2 greater than [pyr13][FSI], while this increases to $\sim$ 10 for [pyr14][TFSI] at lower T. Additional information on the experimental measurement of λ is presented in Figure S7 of the supplementary material.

In Fig. 14, we compare our experimental values for λ of the ionic liquids (0.5 m solutions of Li-salt in the ionic liquids) against that of a standard Li-ion electrolyte (1 mole of Li[PF_6] per liter of a 1:1 ethylene carbonate and dimethyl carbonate mixture) to asses the suitability of our ionic liquids for batteries. The temperature dependence of ionic conductivity is fitted to a form of the Vogel-Tamman-Fulcher relationship,

$$\sigma = \frac{A}{\sqrt{T}} \exp\left(\frac{E_a}{R(T - T_o)}\right), \tag{8}$$

where A, E_a, and T_o are fitted parameters and R is the ideal gas constant. The conductivity of 0.5 m Li[BF_4] in [EMIM][BF_4] and 0.5 m Li[FSI] in [pyr13][FSI] compare favorably with the Li-ion electrolyte at room temperature, but both fall off more rapidly at reduced temperature. λ of 0.5 m Li[TFSI] in [pyr14][TFSI] is nearly an order of magnitude lower than that of the other ionic liquids, as well as that of the standard electrolyte, at low and moderate values of T. It has, however, been suggested that additives might be a possible route to tune ionic conductivity values of potential ionic liquid electrolytes.

We additionally compute room temperature properties especially important for electrochemical applications, which include η_{xy}, the diffusion coefficient of Li^+ (D^{Li^+}), and the Li^+ component of ionic conduction (λ^{Li^+}), for x_{Li^+} in the range 0.05 to 0.33, Fig. 15. While expressions for η_{xy} and D^{Li^+} have been provided, we estimate λ^{Li^+} from a ratio of the diffusion

coefficients and the net ionic conductivity,

$$\lambda^{\mathrm{Li}^+} = \lambda \frac{\mathrm{N}^{\mathrm{Li}^+}\mathrm{D}^{\mathrm{Li}^+}}{\mathrm{N}^+\mathrm{D}^+ + \mathrm{N}^-\mathrm{D}^- + \mathrm{N}^{\mathrm{Li}^+}\mathrm{D}^{\mathrm{Li}^+}} \tag{9}$$

where N^+, N^-, and $\mathrm{N}^{\mathrm{Li}^+}$ are the number of cations, anions, and Li^+ ions, respectively, in our simulation cell. The errors in our computed values of η_{xy}, $\mathrm{D}^{\mathrm{Li}^+}$, and λ^{Li^+} generally range between 10-15%, though our computed value of λ^{Li^+} at $\mathrm{x}_{\mathrm{Li}^+}$ for [pyr14][TFSI] is off by a factor of two, which is a propagation of the previously mentioned underestimation of λ in this system at low-T. We note a few interesting trends with respect to increasing Li-doping, including increasing η_{xy}, decreasing $\mathrm{D}^{\mathrm{Li}^+}$, and a plateau in λ^{Li^+}. For each liquid, η_{xy} and $\mathrm{D}^{\mathrm{Li}^+}$ increases and decreases, respectively, by an order of magnitude as $\mathrm{x}_{\mathrm{Li}^+}$ rises from 0.05 to 0.33. At $\mathrm{x}_{\mathrm{Li}^+} = 0.33$ the [pyr14][TFSI] system has the largest viscosity at 1448 cP, $\sim$4 times larger than the other systems, and lowest $\mathrm{D}^{\mathrm{Li}^+}$ at 0.006×10^{-10}, $\sim$4 times smaller than the other systems. While the increase and decrease in η_{xy} and $\mathrm{D}^{\mathrm{Li}^+}$, respectively, are sensible and likely correspond to the increase in density with $\mathrm{x}_{\mathrm{Li}^+}$ noted in Fig. 10, the plateau in λ^{Li^+} can be attributed to a balance between the diffusion of lithium, which decreases with higher $\mathrm{x}_{\mathrm{Li}^+}$, and the total number $\mathrm{N}_{\mathrm{Li}^+}$, which increases. In terms of λ^{Li^+}, [pyr14][TFSI] again has the poorest performance at 0.03 mS/cm, which is nearly an order of magnitude lower than λ^{Li^+} for [EMIM][BF_4] at 0.26 mS/cm and [pyr13][FSI] at 0.17 mS/cm.

To better understand the error tolerance of our low-T computational measures of transport, we now compare our transport values in Figs. 11, 12, and 15 to those from additional simulations of [pyr14][TFSI] having $\mathrm{x}_{\mathrm{Li}^+} = 0.1$ and 0.25 as performed with *Lucretius*.[49] The *Lucretius* simulations, which are denoted as "luc," use initial configurations uncorrelated to our other simulations and contain 160 pairs. As shown in these figures, $\mathrm{D}^{\mathrm{Li}^+}$, viscosity and λ^{Li^+} from the luc simulations are in good agreement with our standard results derived from LAMMPS, with the largest deviations being in the diffusion of Li^+ and viscosity at low-T (typical deviations being $\sim$ 10-15 %). The simulation statistics, then, so obtained by the

two simulation packages are congruent. The variability in transport is likely less dependent on initial configuration than errors related to the length of simulation time, which is further discussed in Fig. S8 of the supplementary material on the basis of deviations in low-T $\mathrm{D}^{\mathrm{Li}^+}$ over the course of hundreds of nanoseconds of statistical averaging. Thus, we strongly suggest that care be taken to ensure that ample statistics are taken over long simulation times to produce converged transport properties in Li-doped room-T ionic liquids, with hundreds of nanoseconds of simulation statistics being necessary to prevent large errors in transport estimates.

Kinetics of Lithium Transport

It is worthwhile to further analyze the underlying mechanisms that govern the transport, in particular that of Li^+, in our ionic liquid systems. As a first approach, we compare the λ of our liquids, as computed from Eq. 7, with an ideal measure of ionic conduction (λ^{uc}) that does not account for the correlated motion of the ions,

$$\lambda^{uc} = \frac{e^2}{k_B V T} \sum_{\beta=1}^{\mathrm{N}^{ions}} (z^\beta)^2 \mathrm{D}^\beta \mathrm{N}^\beta, \tag{10}$$

where z^β is the net charge of each ionic species β. Expressing the effect of correlated ion motion as the ratio $\alpha = \lambda/\lambda^{uc}$, we provide in Table 2 measures of α for the ionic liquids at $T = 298$ K and selected values of $\mathrm{x}_{\mathrm{Li}^+}$. We find that our estimated α is on the order of both experimental measurements, which have yielded 0.39-0.86 for [pyr13][TFSI] with Li[TFSI][25,60] and 0.7-0.85 for [EMIM][BF_4] with Li[BF_4],[24] as well as alternate MD studies of Li-doped ionic liquids.[20,41,44,45] With increased $\mathrm{x}_{\mathrm{Li}^+}$, we observe a slight increase in α that suggests less correlated ion diffusion.

In order to further probe possible mechanisms of transport, we look to the average resi-

dence time of neighboring ions. This is accomplished by defining a neighbor function ($H^{\beta\gamma}$),

$$H^{\beta\gamma}(R_{ij},t) = \begin{cases} 0, & \text{if } R_{ij} > R_{\beta\gamma}^{|MAX|} \\ 1, & \text{if } R_{ij} \leq R_{\beta\gamma}^{|MAX|} \end{cases} \tag{11}$$

which determines whether the ions i and j of species type β and γ, respectively, are neighbors based on their center of mass separation, R_{ij}, and the average maximum extent of the first solvation shell, $R_{\beta\gamma}^{|MAX|}$, which can be obtained from the g(r). The residence time, then, can be evaluated from the autocorrelation of $H^{\beta\gamma}$,

$$S^{\beta\gamma}(t) = \left\langle \frac{\sum_{i=1}^{N^\beta}\sum_{j=1}^{N^\gamma} H^{\beta\gamma}(R_{ij},t)H^{\beta\gamma}(R_{ij},0)}{\sum_{i=1}^{N^\beta}\sum_{j=1}^{N^\gamma} H^{\beta\gamma}(R_{ij},0)H^{\beta\gamma}(R_{ij},0)} \right\rangle, \tag{12}$$

which exhibits a roughly exponential decay, the average decay time of which is $\tau^{\beta/\gamma}$ between ion species β and γ.

The residence time of Li^+ with anions in each liquid is mapped out in Fig. 16a, which reveals exceptionally long residence times that follow the trend $\tau^{Li/[TFSI]} > \tau^{Li/[BF_4]} > \tau^{Li/[FSI]}$. While $\tau^{Li/-}$ in every liquid increases with increased x_{Li^+}, the relative rate of increase is greatest for [pyr14][TFSI], with $\tau^{Li/[TFSI]}$ at $x_{Li^+} = 0.33$ reaching 100 ns - fully an order of magnitude larger than that of the other liquids. Though a relationship between the two has not been previously established, it appears that the increase in τ between Li^+ and the anions corresponds to a decrease in correlated motion, as given by increasing α. Additionally, T has a marked effect on $\tau^{Li/-}$, shown in Fig. 16b for $x_{Li^+} = 0.10$. $\tau^{Li/-}$ decreases by roughly an order of magnitude as T is increased from 298 K to 393 K, though we note that $\tau^{Li/[FSI]}$ and $\tau^{Li/[BF_4]}$ appear to be converging at 393 K, while $\tau^{Li/[TFSI]}$ is still a factor of two larger.

Intuitively, a longer $\tau^{Li/-}$ at higher x_{Li^+} would suggest a greater correlated motion; however, this would only be the case if ion diffusion rates remained unchanged, which the suppression of D in Fig. 14 clearly contradicts. Alternatively, the suppressed diffusion and long residence time, along with increasing α, could indicate a change in transport mechanism

to one in which diffusion occurs with less correlated motion. Consequently, the primary mechanisms proposed for Li^+ diffusion include the highly correlated vehicular mechanism, where Li^+ moves with its solvation shell, and the hopping mechanism, where Li^+ is pulled through the liquid *via* anion exchange. To compare these mechanisms, we compute the average displacement of Li^+ before an anion exchange event occurs at time $\tau^{Li/-}$ as well as the ratio of Li^+ diffusion before anion exchange ($D_{bax}^{Li^+}$) to D^{Li^+}; a small ratio of $D_{bax}^{Li^+}$ to D^{Li^+} implies more importance of anion exchange on diffusion. In Table 3, we provide $D_{bax}^{Li^+}/D^{Li^+}$ at selected conditions along with the Li^+ displacement measured in numbers of average anion radii, $N^{\langle R \rangle}$. With increasing x_{Li^+}, we see a shift to lower $D_{bax}^{Li^+}/D^{Li^+}$ as well as a lower $N^{\langle R \rangle}$, indicating that anion exchange contributes more greatly to net Li^+ diffusion and that Li^+ is displaced on average less before an anion exchange event, supporting the increase of α in Table 2. Based on a comparison of the magnitudes of $D_{bax}^{Li^+}/D^{Li^+}$, the importance of the vehicular mechanism follows [EMIM][BF_4] > [pyr13][FSI] > [pyr14][TFSI], which also implies anion exchange becomes more important as anion size increases.

As a final evaluation of transport in Li-doped ionic liquids, we look at the influence of Li^+ clusters on both $\tau^{Li/-}$ and D^{Li^+}. As shown in Table 4, we compute $\tau^{Li/-}$ and D^{Li^+} for single Li^+ ions (denoted clusters of one, $N_{Li^+} = 1$) and cluster Li^+ with common bridging anions ($N_{Li^+} > 1$); the average duration of the clusters is also quoted on the basis of the Li-Li residence time ($\tau^{Li/Li}$). We initially note that the magnitude of $\tau^{Li/Li}$ with respect to ionic liquid follows the order previously established for $\tau^{Li/-}$ and that in all cases $\tau^{Li/-}$ is larger for $N_{Li^+} > 1$ systems than $N_{Li^+} = 1$ systems. The magnitude of this effect, however, varies markedly by system, with $\tau^{Li/-}$ for $N_{Li^+} > 1$ clusters being a factor of ~ 2 and $\sim 3/2$ larger than $\tau^{Li/-}$ for $N_{Li^+} = 1$ in [pyr14][TFSI] and [pyr13][FSI], respectively, while both Li^+-Anion residence times are comparable for [EMIM][BF_4]. Associated with this increase in cluster residence time is an increase by a factor of ~ 1.5 in D^{Li^+} for $N_{Li^+} = 1$ when compared to $N_{Li^+} > 1$ systems in [pyr14][TFSI] and [pyr13][FSI], with [EMIM][BF_4] again being the exception with comparable D^{Li^+} independent of cluster size. Upon closer

inspection of the structures associated with these values, it is noted that the increase in $\tau^{\mathrm{Li}/-}$ for $\mathrm{N_{Li^+}} > 1$ systems can almost completely be attributed to the long-lived bridging anions (given by coordination > 1 in Fig. 9), while anions on the exterior of the cluster (given by 1-coordination in Fig. 9) are exchanged at rates comparable to those associated with $\mathrm{N_{Li^+}} = 1$ clusters.

Conclusions

We have presented an comprehensive investigation of the structure, thermodynamics and transport properties of the ionic liquids [pyr14][TFSI], [pyr13][FSI], and [EMIM][BF_4] as a function of Li-salt doping and T. Molecular dynamics simulation are performed using the polarizable force field, APPLE&P. An analysis of the influence of $\mathrm{x_{Li^+}}$ on ionic liquid structure reveals a complex binding environment in which Li^+ prefers 4-coordination, which is generally mediated through 4 anions having κ^1 binding, except for the case of [pyr14][TFSI] which prefers a 3 anion coordination consisting of 2 κ^1 bonds and 2 κ^2 bonds. A result of adding Li^+ past a threshold value of $\mathrm{x_{Li^+}} = 0.05$ is the mutual coordination of lithium ions to the same anion, resulting in lithium clusters. The clustering effect has a significant impact on both the structure and transport properties of our ionic liquids, reducing the prevalence of κ^2 binding in [pyr14][TFSI] and [pyr13][FSI] as well as slowing the dynamics of the liquids through a substantial increase in density.

We have evaluated the expected performance of each electrolyte based on their viscosity, diffusion, and ionic conduction as well as the individual contribution of Li^+ to the ionic conduction. MD simulation predictions were found to be in good agreement with pulsed field gradient spin-echo NMR measurements of diffusion and electrochemical impedance spectroscopy measurements of ionic conductivity for the neat ionic liquids and 0.5 m solutions of Li-salt in the ionic liquids. With increasing Li-salt doping, all liquids exhibit the same general trends of increasing viscosity and decreasing diffusion and ionic conductivity. The

influence of Li-salt doping is notable, with our $T = 298$ K systems showing a net increase of η_{xy} and a net decrease of D^{Li^+} of an order of magnitude as x_{Li^+} increases from 0.05 to 0.33. Contrasting this behavior, increasing Li-salt doping causes λ^{Li^+} to saturate after a threshold of $x_{Li^+} = 0.15$, which is shown to be the combined influence of decreasing diffusion and increasing number of Li^+. Comparing the properties of our potential electrolytes across the entire range of x_{Li^+}, a correlation between anion size and transport emerges, with smaller anions having smaller viscosity and higher rates of Li^+ transport. The liquid with the largest anion, [pyr14][TFSI], has the highest viscosity, being a factor of ∼4 larger than the other liquids, while D^{Li^+} is a factor of ∼4 lower. Without question, [pyr14][TFSI] exhibits the lowest Li^+ contribution to ionic conduction, λ^{Li^+} being roughly an order of magnitude lower than that of the other liquids, and [EMIM][BF_4] has the highest λ^{Li^+}, reaching values of 0.30 mS/cm at high x_{Li^+}, though [pyr13][FSI] is a close lower bound at 0.17 mS/cm. It should additionally be noted that our room-T simulation results of Li-doped ionic liquids demonstrate the necessity of long MD simulation runs (∼ 200 ns) to obtain accurate measures of transport.

An analysis of the kinetics of Li^+ transport has been performed on the basis of residence times, $\tau^{Li/-}$, of anions with Li^+. At $T = 298$ K, Li[TFSI] binding persists up to 100 ns at x_{Li^+} =0.33. Li[FSI] and Li[BF_4] binding, on the other hand, have much smaller values of $\tau^{Li/-}$ at 8 ns and 17 ns, respectively. Increasing T reduces the residence times dramatically, exhibiting an order of magnitude decrease from 298 K to 393 K. Using $\tau^{Li/-}$ along with diffusion data, we have additionally investigated the competition between the hopping mechanism and the vehicular mechanism in the transport of Li^+. The contribution of Li^+/anion exchange to Li^+ diffusion is estimated to be less that 40 % and increases with both increasing x_{Li^+} and anion size ([TFSI] > [FSI] > [BF4]).

Finally, we briefly note that Li^+ transport is governed by the correlated influence of anion size, anion binding strength, and liquid density. For instance, [pyr14][TFSI] and [pyr13][FSI] are similar ionic liquids in terms of structure, though the residence time of Li^+ with [TFSI]

is roughly an order of magnitude larger, which inevitably leads to slower diffusion of Li^+. It is attractive to attribute this to the bonding energy, which is stronger for [TFSI] than [FSI]; however, bonding alone does not completely govern $\tau^{Li/-}$, as $[BF_4]$ has the strongest binding energy with a $\tau^{Li/-}$ several times smaller than that of [TFSI]. What, then, emerges is a picture where strong anion binding, large anion size, and high density create a prolonged Li[TFSI] solvation structure that leads to slow transport. While $Li[BF_4]$ has strong binding, the small anion size and low density allow rapid diffusion of Li^+ with its solvation shell as well as a high rate of anion exchange. Finally, the weak binding of Li[FSI] and intermediate density of [pyr13][FSI] seem to allow a greater rate of anion exchange and result in higher Li^+ mobility.

Acknowledgement

This work was supported by funding from the NASA Aeronautics Research Institute (NARI) Seedling program.

References

(1) Armand, M.; Tarascon, J. M. *Nature* **2008**, *451*, 652–657.

(2) Scrosati, B.; Garche, J. *J. Power Sources* **2010**, *195*, 2419–2430.

(3) Goodenough, J. B.; Kim, Y. *Chem. Mater* **2010**, *22*, 587–603.

(4) Ellis, B. L.; Lee, K. T.; Nazar, L. F. *Chem. Mater.* **2010**, *22*, 691–714.

(5) Matsumoto, H.; Sakaebe, H.; Tatsumi, K.; Kikuta, M.; Ishiko, E.; Kono, M. *J. Power Sources* **2006**, *160*, 1308–1313.

(6) Schweikert, N.; Hofmann, A.; Schulz, M.; Scheuermann, M.; Boles, S. T.; Hanemann, T.; Hahn, H.; Indris, S. *J. Power Sources* **2013**, *228*, 237–243.

(7) Xu, J.; Yang, J.; NuLi, Y.; Wang, J.; Zhang, Z. *J. Power Sources* **2006**, *160*, 621–626.

(8) Basile, A.; Hollenkamp, A. F.; Bhatt, A. I.; O'Mullane, A. P. *Electrochem. Commun.* **2013**, *27*, 69–72.

(9) Howlett, P. C.; MacFarlane, D. R.; Hollenkamp, A. F. *Electrochem. Solid State Lett.* **2004**, *5*, A97–A101.

(10) Bhatt, A. I.; Best, A. S.; Huang, J.; Hollenkamp, A. F. *J. Electrochem. Soc.* **2010**, *157*, A66.

(11) Best, A. S.; Bhatt, A. I.; Hollenkamp, A. F. *J. Electrochem. Soc.* **2010**, *157*, A903–A911.

(12) Bhattacharyya, R.; Key, B.; Chen, H.; Best, A. S.; Hollenkamp, A. F.; Grey, C. P. *Nature. Mater.* **2010**, *9*, 504–510.

(13) Wang, H.; Liu, S.; Huang, K.; Yin, X.; Liu, Y.; Peng, S. *Int. J. Electrochem. Sci.* **2012**, *7*, 1688–1698.

(14) Wang, Y.; Zaghib, K.; Guerfi, A.; Bazito, F. F. C.; Torresi, R. M.; Dahn, J. R. *Electrochim. Acta* **2007**, *52*, 6346–6352.

(15) Saint, J.; Best, A. S.; Hollenkamp, A. F.; Kerr, J.; Shin, J.-H.; Doeff, M. M. *J. Electrochem. Soc.* **2008**, *155*, A127–A180.

(16) Lane, G. H.; Best, A. S.; MacFarlane, D. R.; Forsyth, M.; Hollenkamp, A. F. *Electrochim. Acta* **2010**, *55*, 2210–2215.

(17) Tokuda, H.; Hayamizu, K.; Ishii, K.; Abu Bin Hasan Susan, M.; Watanabe, M. *J. Phys. Chem. B* **2004**, *108*, 16593–16600.

(18) Tokuda, H.; Hayamizu, K.; Ishii, K.; Abu Bin Hasan Susan, M.; Watanabe, M. *J. Phys. Chem. B* **2005**, *109*, 6103–6110.

(19) Tokuda, H.; Ishii, K.; Abu Bin Hasan Susan, M.; Tsuzuki, S.; Hayamizu, K.; Watanabe, M. *J. Phys. Chem. B* **2006**, *110*, 2833–2839.

(20) Borodin, O.; Gorecki, W.; Smith, G. D.; Armand, M. *J. Phys. Chem. B* **2010**, *114*, 6786–6798.

(21) Castiglione, F.; Ragg, E.; Mele, A.; Appetecchi, G. B.; Montanino, M.; Passerini, S. *J. Phys. Chem. Lett.* **2011**, *2*, 153–157.

(22) Zhou, Q.; Henderson, W.; Appetecchi, G.; Montanino, M.; Passerini, S. *J. Phys. Chem. B* **2008**, *112*, 13577–13580.

(23) Zhou, Q.; Boyle, P. D.; Malpezzi, L.; Mele, A.; Shin, J.-H.; Passerini, S.; Henderson, W. A. *Chem. Mater* **2011**, *23*, 4331–4337.

(24) Hayamizu, K.; Aihara, Y.; Nakagawa, H.; Nukuda, T.; Price, W. S. *J. Phys. Chem. B* **2004**, *108*, 19527–19532.

(25) Nicotera, I.; Oliviero, C.; Henderson, W. A.; Appetecchi, G. B.; Passerini, S. *J. Phys. Chem. B* **2005**, *109*, 22814–22819.

(26) Fujii, K.; Seki, S.; Fukuda, S.; Takamuku, T.; Kohara, S.; Kameda, Y.; Umebayashi, Y.; Ishiguro, S. *J. Mol. Liq.* **2008**, *143*, 64–69.

(27) Fujii, K.; Hamano, H.; Doi, H.; Song, X.; Tsuzuki, S.; Hayamizu, K.; Seki, S.; Kameda, Y.; Dokko, K.; Watanabe, M.; Umebayashi, Y. *J. Phys. Chem. C* **2013**, *117*, 19314–19324.

(28) Umebayashi, Y.; Hamamo, H.; Seki, A.; Minofar, B.; Fujii, K.; Hayamizu, K.; Tsuzuki, S.; Kameda, Y.; Kohara, S.; Watanabe, M. *J. Phys. Chem. B* **2011**, *115*, 12179–12191.

(29) Fujii, K.; Fujimori, T.; Takamuku, T.; Kanzaki, R.; Umebayashi, Y.; Ishiguro, S. *J. Phys. Chem. B* **2006**, *110*, 8179–8183.

(30) Umebayashi, Y.; Mitsugi, T.; Fukuda, S.; Fujimori, T.; Fujii, K.; Kanzaki, R.; Takeuchi, M.; Ishiguro, S. *J. Phys. Chem. B* **2007**, *111*, 13028–13032.

(31) Herstedt, M.; Smirnov, M.; Johansson, P.; Chami, M.; Grondin, J.; Servant, L.; Lassègues, J. C. *J. Raman Spectrosc.* **2005**, *36*, 762–770.

(32) Lassègues, J.-C.; Grondin, J.; Aupetit, C.; Johansson, P. *J. Phys. Chem. A* **2009**, *113*, 305–314.

(33) Borodin, O.; Smith, G. D. *J. Phys. Chem. B* **2006**, *110*, 6293–6299.

(34) Borodin, O. *J. Phys. Chem. B* **2009**, *113*, 11463–11478.

(35) Liu, H.; Maginn, E.; Visser, A. E.; Bridges, N. J.; Fox, E. B. *Ind. Eng. Chem. Res.* **2012**, *51*, 7242–7254.

(36) Canongia Lopes, J. N. A.; Padau, A. A. H. *J. Phys. Chem. B* **2006**, *110*, 7485–7489.

(37) Hunt, P. A. *Mol. Simul.* **2006**, *32*, 1–10.

(38) Borodin, O.; Smith, G. D.; Kim, H. *J. Phys. Chem. B* **2009**, *113*, 4771–4774.

(39) Borodin, O.; D., S. G. *J. Phys. Chem. B* **2006**, *110*, 11481–11490.

(40) Borodin, O.; Smith, G. D. *J. Phys. Chem. B* **2006**, *110*, 6279–6292.

(41) Borodin, O.; D., S. G.; Henderson, W. *J. Phys. Chem. B* **2006**, *110*, 16879–16886.

(42) Liu, H.; Maginn, E. *J. Chem. Phys.* **2013**, *139*, 114508.

(43) Méndez-Morales, T.; Carrete, J.; Bouzón-Capelo, S.; Pérez-Rodriguez, M.; Cabeza, O.; Gallego, L. J.; Varela, L. M. *J. Phys. Chem. B* **2013**, *117*, 3207–3220.

(44) Li, Z.; Smith, G. D.; Bedrov, D. *J. Phys. Chem. B* **2012**, *116*, 12801–12809.

(45) Solano, C. J. F.; Jeremias, S.; Paillard, E.; Beljonne, D.; Lazzaroni, R. *J. Chem. Phys.* **2013**, *139*, 034502.

(46) Niu, S.; Cao, Z.; Li, S.; Yan, T. *J. Phys. Chem. B* **2010**, *114*, 877–881.

(47) Markevich, E.; Baranchugov, V.; Aurbach, D. *Electrochem. Commun.* **2006**, *8*, 1331–1334.

(48) Plimpton, S. *J. Comp. Phys.* **1995**, *117*, 1–19, see `http://lammps.sandia.gov`.

(49) Ayyagari, C.; Bedrov, D.; Borodin, O.; Smith, G. D. simulation code see `http://www.eng.utah.edu/gdsmith/lucretius.html`.

(50) Tuckerman, M.; Berne, B. J.; Martyna, G. J. *J. Chem. Phys.* **1992**, *97*, 1990.

(51) Qian, X.; Gu, N.; Cheng, Z.; Yang, X.; Wang, E.; Dong, S. *Electrochimica Acta* **2001**, *46*, 1829–1836.

(52) Song, J. Y.; Wang, Y.; Wan, C. *J. Electrochem. Soc.* **2000**, *147*, 3219–3225.

(53) See supplementary material for additional details on lithium binding and dynamics and on the experiments.

(54) Fujii, K.; Seki, S.; Fukuda, S.; Kanzaki, R.; Takamuku, T.; Umebayashi, Y.; Ishiguro, S. *J. Phys. Chem. B* **2007**, *111*, 12829.

(55) Montiero, M. J.; Bazito, F. F. C.; Siqueira, L. J. A.; Ribiero, M. C. C.; Torresi, R. M. *J. Phys. Chem. B* **2008**, *112*, 2102–2109.

(56) Nowinski, J. L.; Lightfoot, P.; Bruce, P. G. *J. Mater. Chem.* **1994**, *4*, 1579–1580.

(57) Beran, M.; Příhoda, J.; Žák, Z.; Černík, M. *Polyhedron* **2006**, *25*, 1292–1298.

(58) Xue, L.; Padgett, C. W.; DesMarteau, D. D.; Pennington, W. T. *Solid State Sci.* **2002**, *4*, 1535–1545.

(59) Bauschlicher Jr., C. W.; Haskins, J. B.; Bucholz, E. W.; Monk, J. D.; Lawson, J. W. *J. Chem. Phys.* to be submitted.

(60) Bayley, P. M.; Lane, G. H.; Lyons, L. J.; MacFarlane, D. R.; Forsyth, M. *J. Phys. Chem. C* **2010**, *114*, 20569–20576.

(61) Shiflett, M. B.; Yokozeki, A. J. *J. Chem. Eng. Data* **2007**, *52*, 1302–1306.

Table 1: Anions and atoms coordinated to Li^+ at $T = 298$ K.

	[pyr14][TFSI]		[pyr13][FSI]		[EMIM][BF_4]	
x_{Li^+}	n^{Li^+} ($[TFSI]^-$)	n^{Li^+} (O)	n^{Li^+} ($[FSI]^-$)	n^{Li^+} (O)	n^{Li^+} ($[BF_4]^-$)	n^{Li^+} (F)
0.05	3.3	4.1	4.0	4.1	4.0	4.2
0.15	3.5	4.1	4.1	4.2	4.0	4.2
0.33	3.6	4.1	4.4	4.3	4.1	4.2

Table 2: Ratio of ionic conductivity to uncorrelated ionic conductivity (α) at $T = 298$ K.

x_{Li^+}	$\alpha^{[pyr14][TFSI]}$	$\alpha^{[pyr13][FSI]}$	$\alpha^{[EMIM][BF_4]}$
0.05	0.64	0.57	0.71
0.15	0.72	0.64	0.78
0.33	0.85	0.73	0.82

Table 3: Ratio of the $T = 298$ K diffusion of Li^+ before anion exchange ($D^{Li^+}_{bax}$) to the total diffusion of Li^+ (D^{Li^+}). The distance that Li^+ travels before exchanging anions, as measured in numbers of ionic liquid anion radii ($N^{\langle R \rangle}$), is given as reference.

	[pyr14][TFSI]		[pyr13][FSI]		[EMIM][BF_4]	
x_{Li^+}	$D^{Li^+}_{bax}/D^{Li^+}$	$N^{\langle R \rangle}$	$D^{Li^+}_{bax}/D^{Li^+}$	$N^{\langle R \rangle}$	$D^{Li^+}_{bax}/D^{Li^+}$	$N^{\langle R \rangle}$
0.05	0.69	4.4	0.81	3.7	0.89	6.1
0.10	0.66	4.2	0.85	2.4	1.07	5.8
0.33	0.59	3.5	0.73	2.0	0.91	3.9

Table 4: Determination of the influence of clustering on Li^+-Anion residence time ($\tau^{Li/-}$) and Li^+ diffusion (D^{Li^+}) for single Li-ions ($N_{Li^+} = 1$) and those belonging to clusters ($N_{Li^+} > 1$) in ionic liquids having $x_{Li^+} = 0.1$ at $T = 298$ K.

	$\tau^{Li/Li}$ (ns)	$\tau^{Li/-}(N_{Li^+} = 1)$ (ns)	$\tau^{Li/-}(N_{Li^+} > 1)$ (ns)	$D^{Li^+}(N_{Li^+} = 1)$ ($10^{-10}m^2/s$)	$D^{Li^+}(N_{Li^+} > 1)$ ($10^{-10}m^2/s$)
[pyr14][TFSI]	81.3	18.3	41.1	0.034	0.024
[pyr13][FSI]	8.3	4.6	6.8	0.083	0.053
[EMIM][BF_4]	27.7	11.6	12.0	0.078	0.081

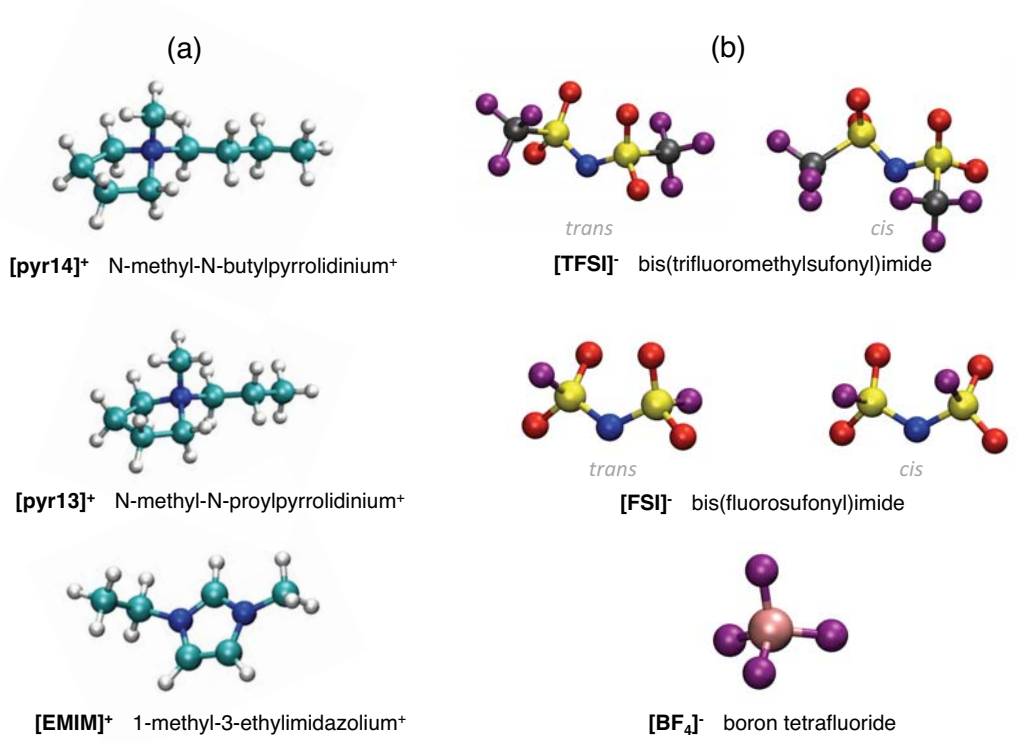

Figure 1: Representation of the cations (a) and anions (b) of the three ionic liquids considered in this work: [pyr14][TFSI], [pyr13][FSI], and [EMIM][BF_4].

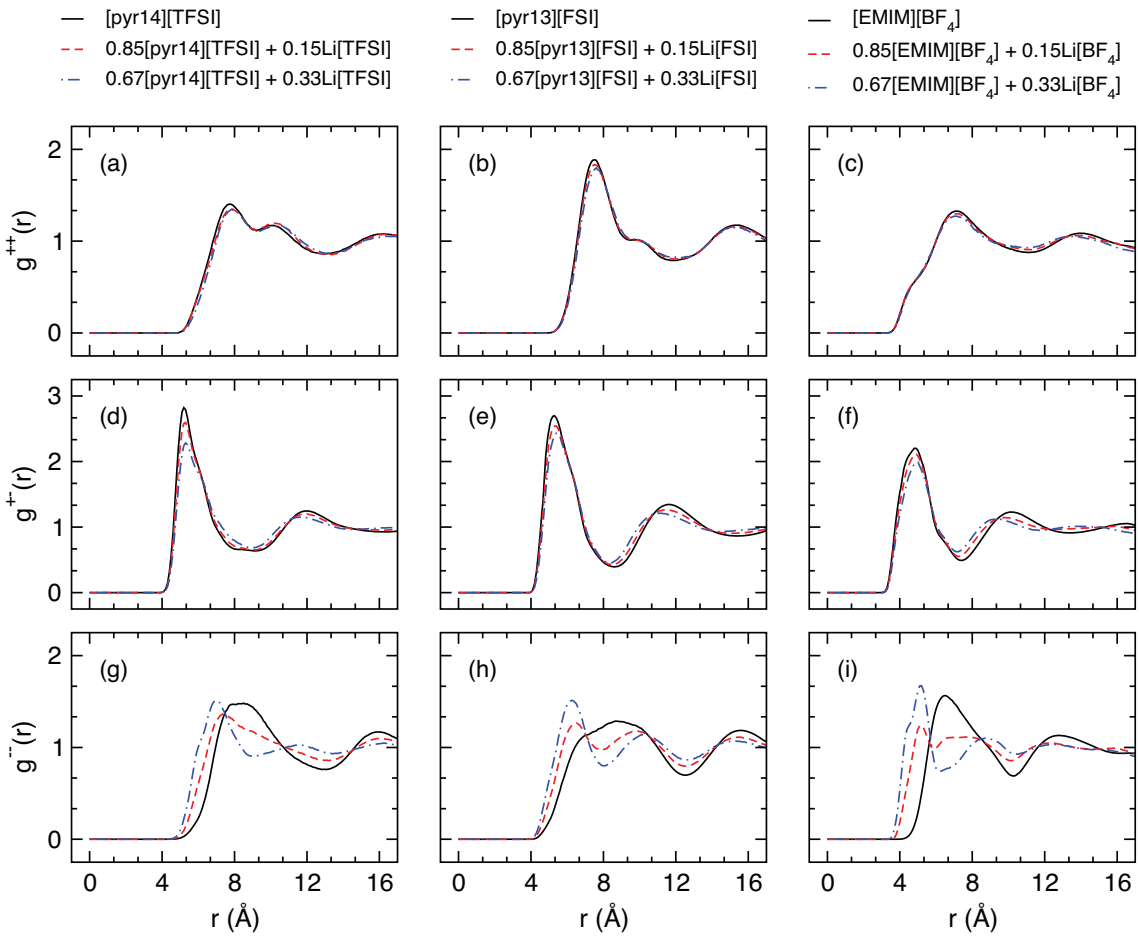

Figure 2: $T = 298$ K radial distribution functions for ionic liquid ions as a function of Li-salt doping. Distributions are provided for cations with other cations (g^{++}), cations with anions (g^{+-}), and anions with anions (g^{--}) for (a,d,e) [pyr14][TFSI], (b,e,h) [pyr13][FSI], and (c,f,i) [EMIM][BF_4].

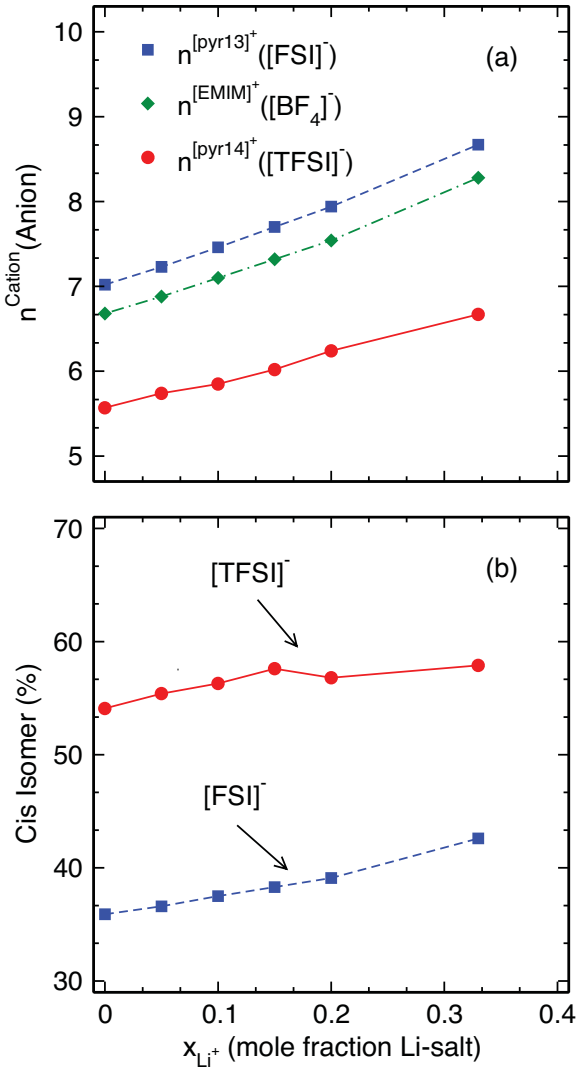

Figure 3: (a) Average number of anion neighbors to each ionic liquid cation, n^{cation}(anion), and (b) probability of cis and trans conformations of anions in the [pyr14][TFSI] and [pyr13][FSI] systems a function of Li-salt doping.

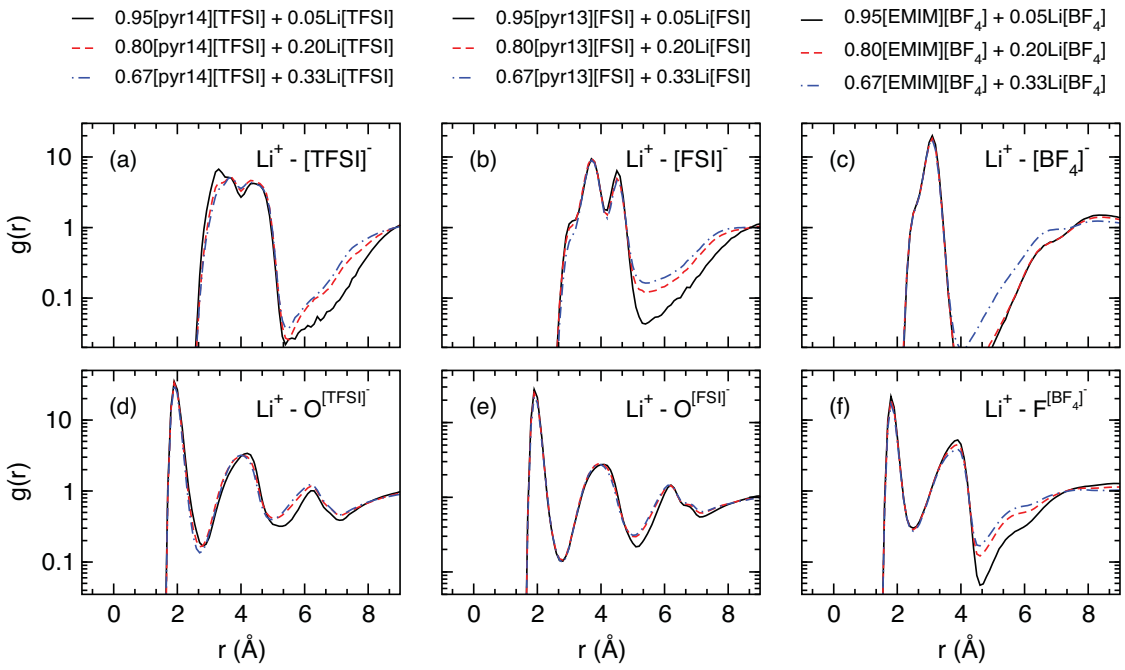

Figure 4: Radial distributions functions of (a-c) Li^+ with anions as well as (d-e) Li^+ with atomic binding sites on the respective anions at $T = 298$ K and as a function of x_{Li^+} for our ionic liquid systems.

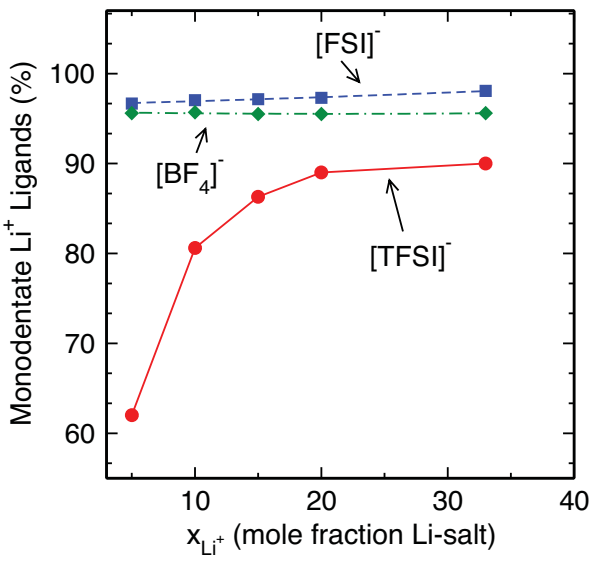

Figure 5: Proportion of Li^+ ligand anions having monodentate bonds as a function of Li-salt doping at $T = 298$ K.

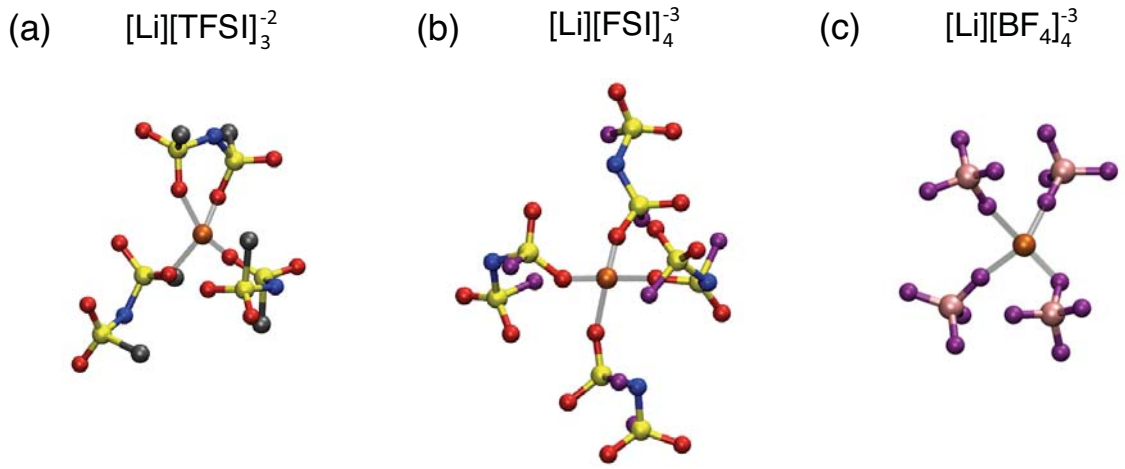

Figure 6: Most likely Li^+ coordination complexes found in (a) [pyr14][TFSI], (b) [pyr13][FSI], and (c) [EMIM][BF_4] at $T = 298$ K and $x_{Li^+} = 0.05$.

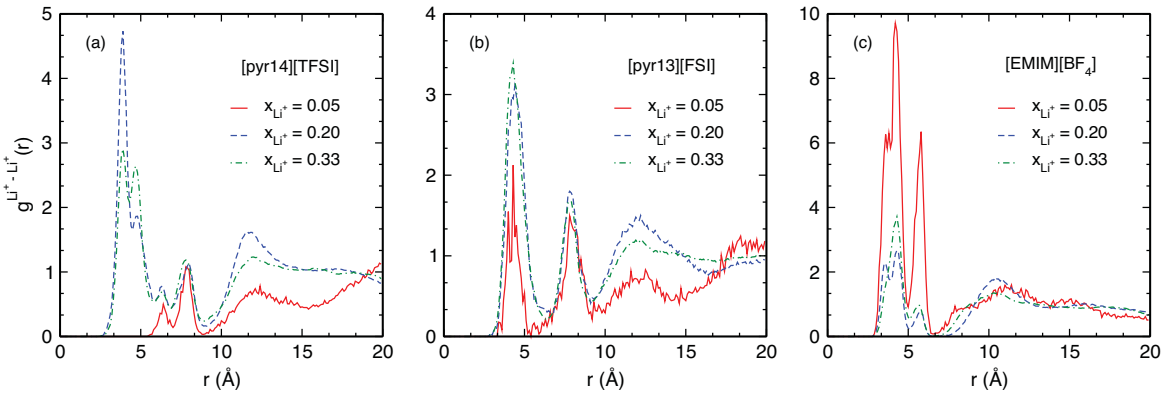

Figure 7: Radial distribution function of Li^+ ions with other Li^+ ions for [pyr14][TFSI], [pyr13][FSI], and [EMIM][BF_4] at $T = 298$ K. The evolution of a large peak at 4 Å indicates formation of clusters.

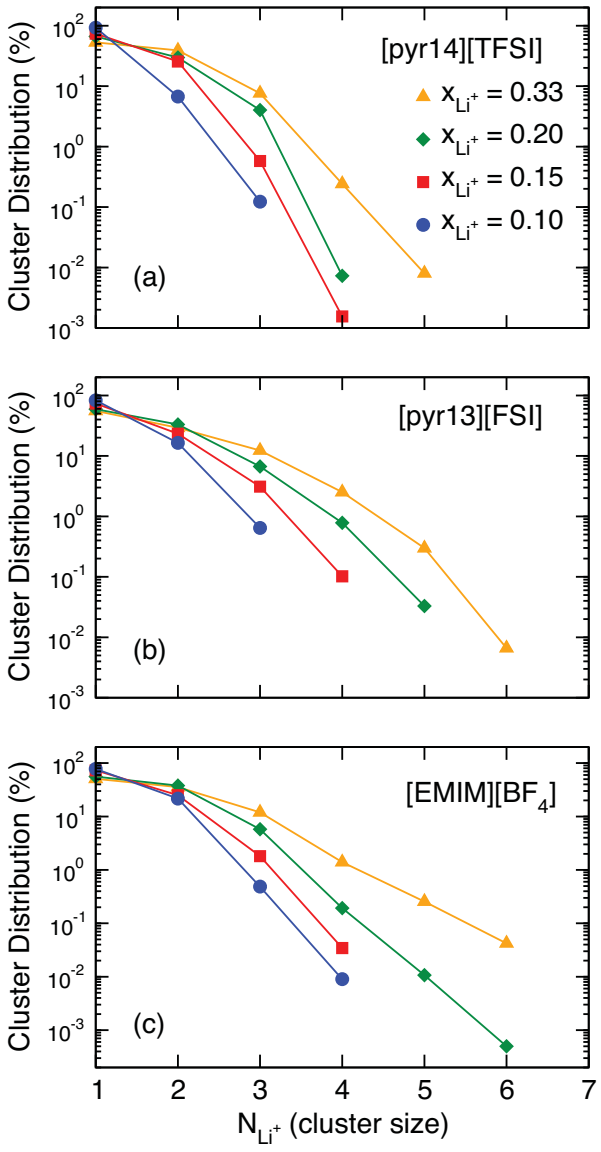

Figure 8: Li-cluster size statistics given as a function of cluster size at $T = 298$ K for (a) [pyr14][TFSI], (b) [pyr13][FSI], and (c) [EMIM][BF_4].

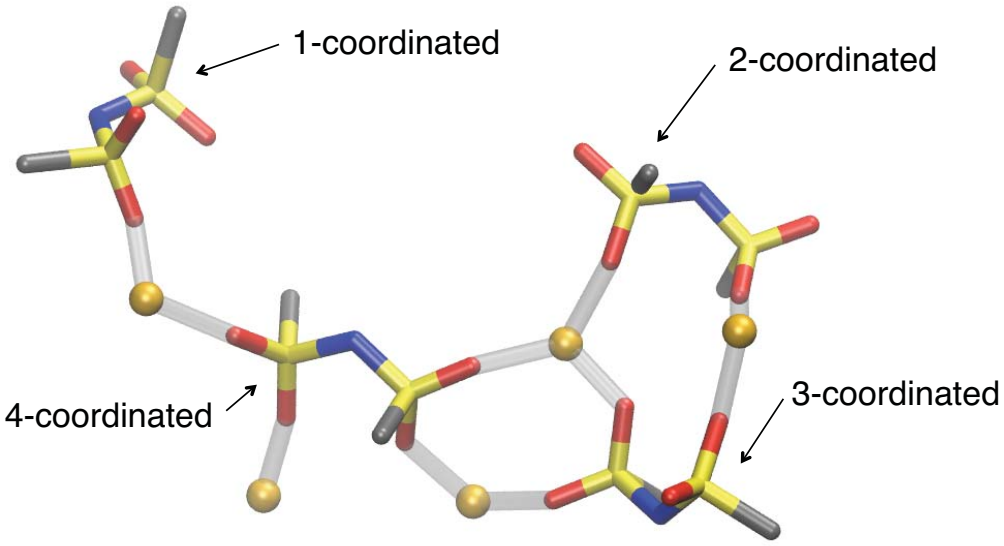

Figure 9: Representative configuration of a lithium cluster taken from a $T = 298$ K [pyr14][TFSI] system having x_{Li^+} =0.33 (F atoms removed for clarity).

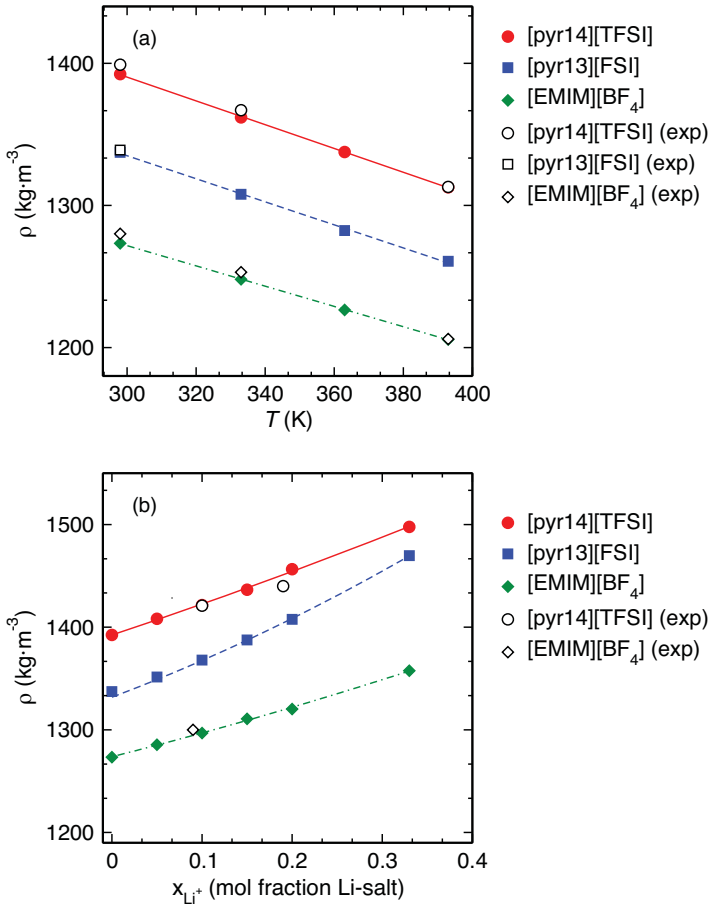

Figure 10: Density of (a) neat ionic liquids as a function of system T and (b) ionic liquids at $T = 298$ K as a function of Li-salt doping. MD simulations (filled symbols) are compared to available experimental measures(open symbols).[19,26,61]

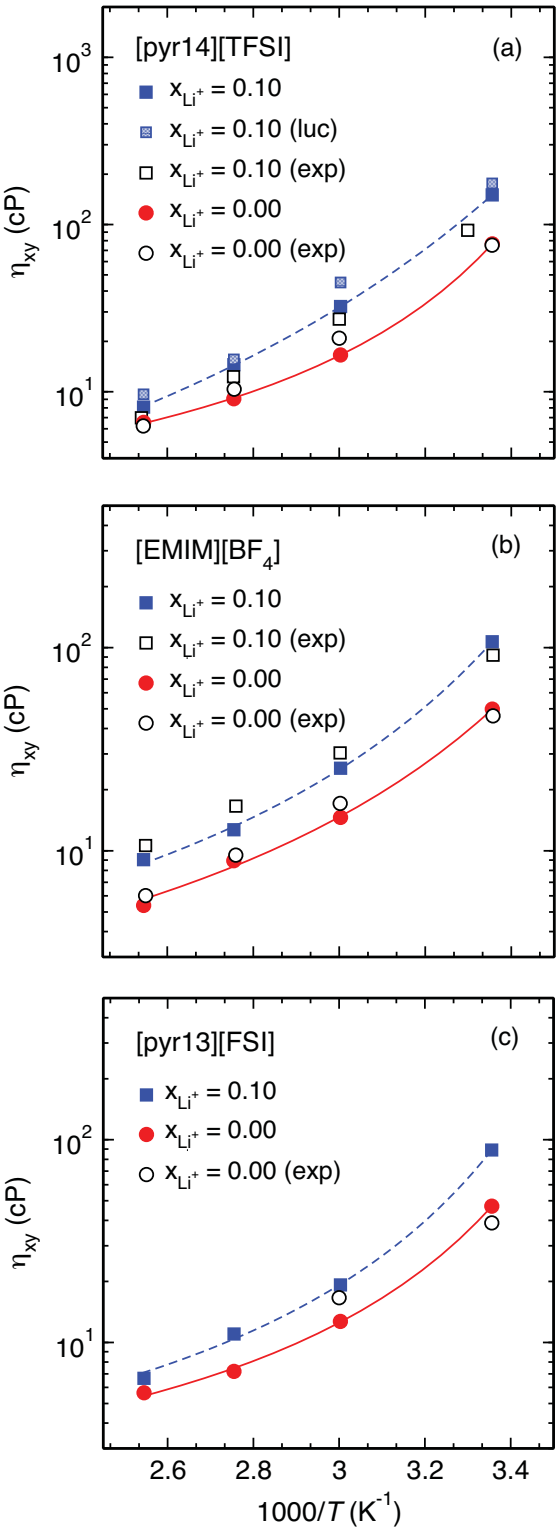

Figure 11: Shear viscosity of (a) [pyr14][TFSI], (b) [EMIM][BF_4], and (c) [pyr13][FSI] for neat systems and those having $x_{Li^+} = 0.10$ as a function of T. Experimental comparisons are included for both systems.[19,22,24,45]

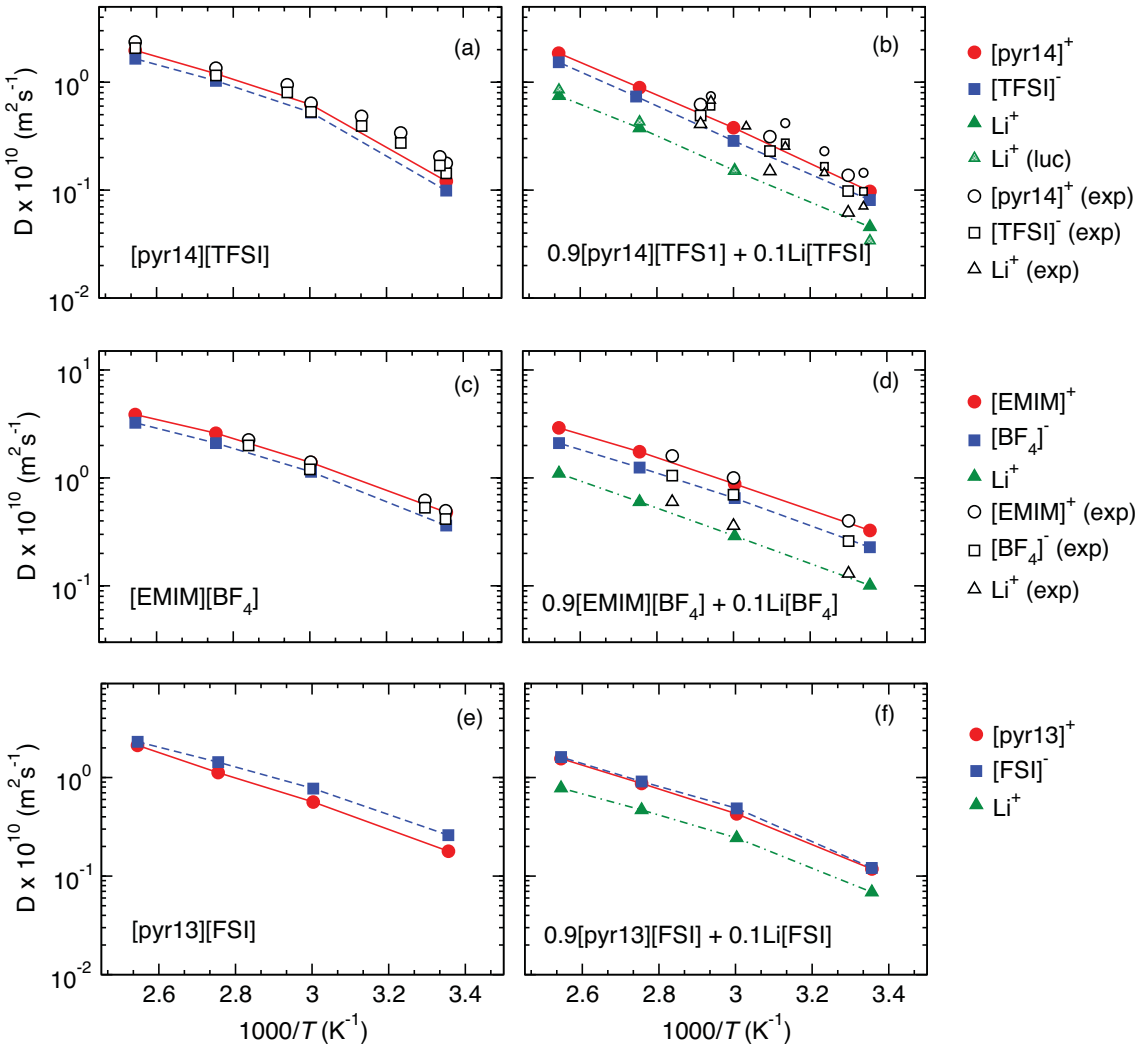

Figure 12: Diffusion coefficients for [pyr14][TFSI] in both (a) the neat form and (b) that having $x_{Li^+} = 0.10$, [EMIM][BF_4] in both (c) the neat form and (d) that having $x_{Li^+} = 0.10$, and [pyr13][FSI] in both (e) the neat form and (f) that having $x_{Li^+} = 0.10$ as a function of T. MD simulation results (solid symbols) are compared with available experiments (outlined symbols).[19,21,24,45]

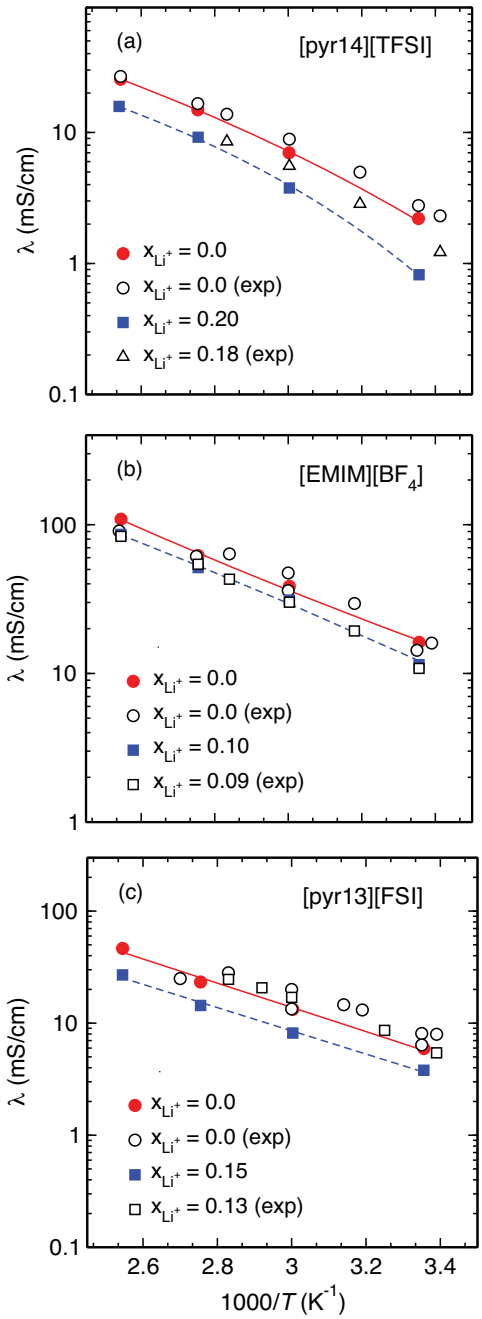

Figure 13: Ionic conduction of (a) [pyr14][TFSI] in both the neat form and that having $x_{Li^+} = 0.20$, (b) [EMIM][BF_4] in both the neat form and that having $x_{Li^+} = 0.10$, and (c) [pyr13][FSI] in both the neat form and that having $x_{Li^+} = 0.15$. MD simulation results (solid symbols) are compared to experimental measures (outlined symbols).[5,19,22,24,53]

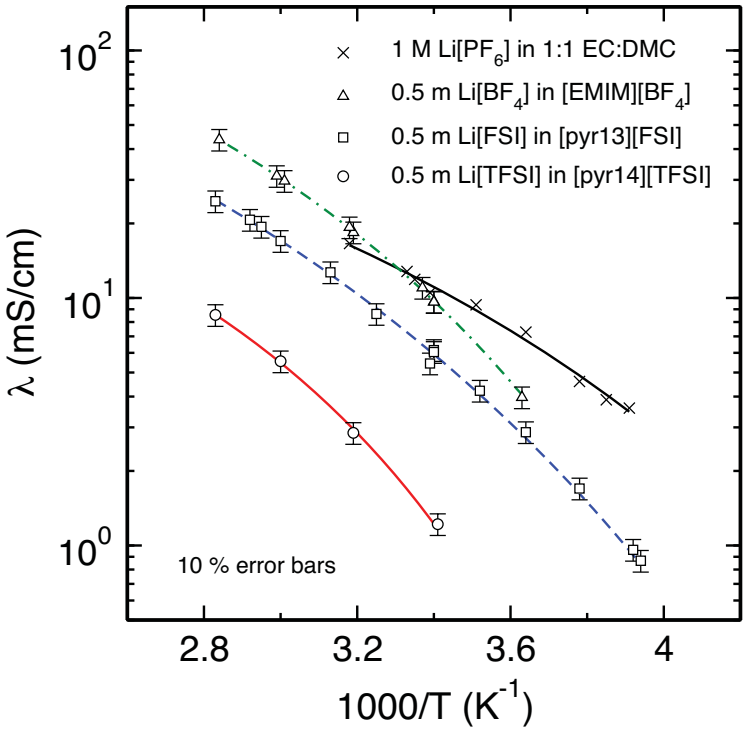

Figure 14: Comparison of experimental measures of λ for 0.5 m Li[BF_4] in [EMIM][BF_4], 0.5 m Li[FSI] in [pyr13][FSI], and 0.5 m Li[TFSI] in [pyr14][TFSI]. Experimental measures of λ for 1 M Li[PF_6] in 1:1 ethylene carbonate:dimethyl carbonate (EC:DMC), a typical Li-ion electrolyte, are also included.

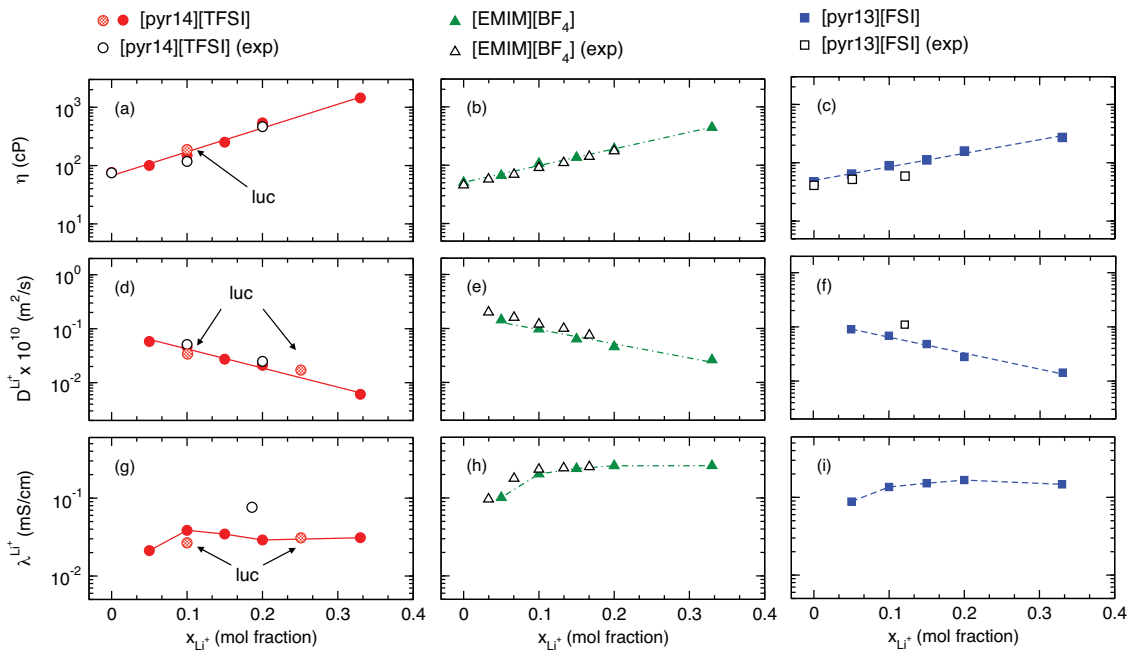

Figure 15: Li-doping dependence of the $T = 298$ K transport properties, (a-c) shear viscosity, (d-f) lithium diffusion, and (g-i) the lithium contribution to ionic conduction, for the three ionic liquids considered in this work. MD simulation results (solid symbols) are compared to available experiments (outlined symbols).[5,10,14,19,21,24,53]

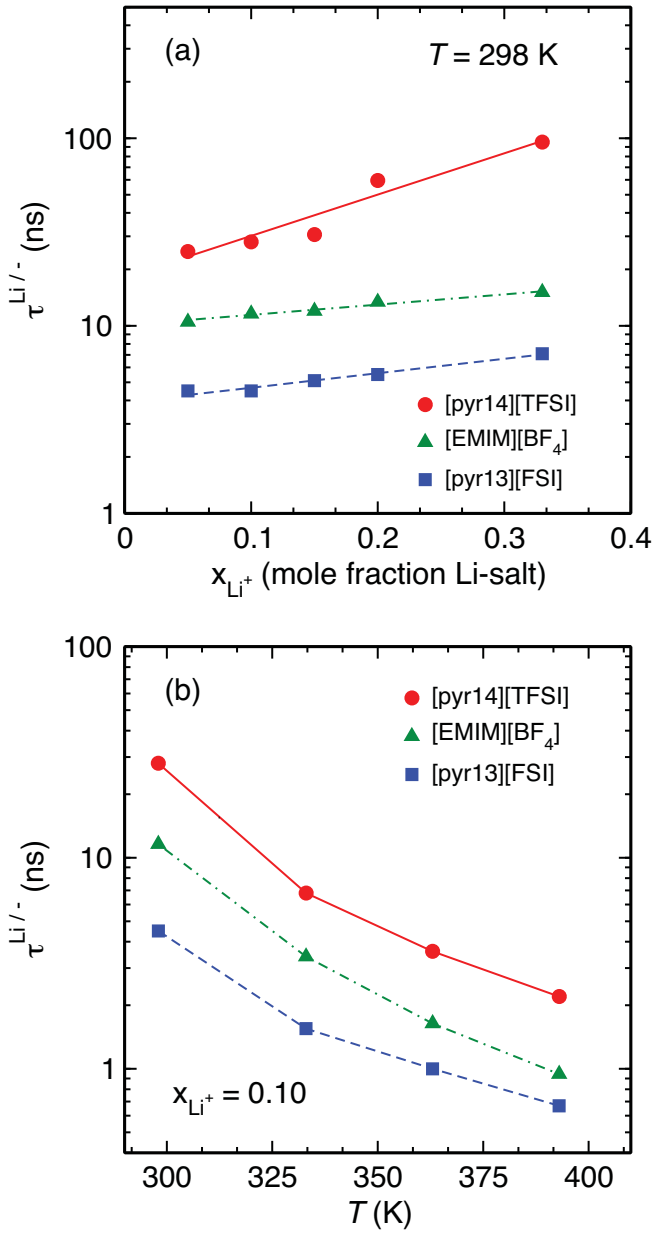

Figure 16: Residence time ($\tau^{\mathrm{Li}/-}$) of Li^+ with ionic liquid anions, given (a) as a function of $\mathrm{x}_{\mathrm{Li}^+}$ at $T = 298$ K and (b) as a function of T at $\mathrm{x}_{\mathrm{Li}^+} = 0.10$.

SUPPLEMENTARY MATERIAL

Contents

1. Structural Analysis

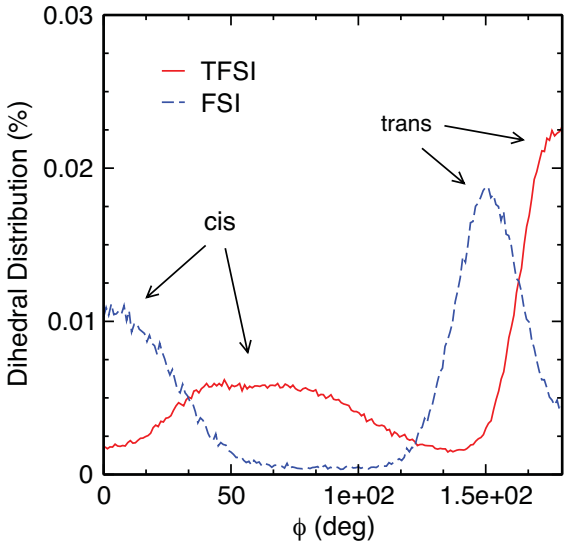

Figure S1. Distribution of the C-S–S-C dihedral and the F-S–S-F dihedral in $[TFSI]^-$ and $[FSI]^-$, respectively, at $T = 298$ K. Values of ϕ close to 180° represent trans conformations, while smaller values represent cis conformations.

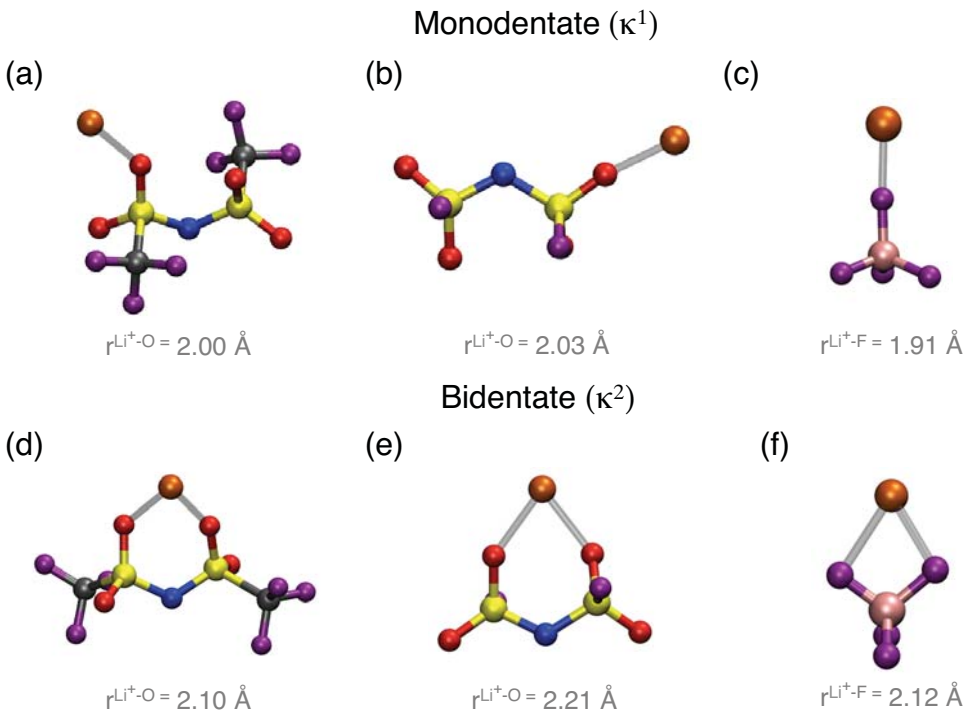

FIGURE S2. Depiction of monodentate (a-c) and bidentate (d-f) binding states for Li[TFSI], Li[FSI], and Li[BF_4]. Average bond distances at T = 298 K are included.

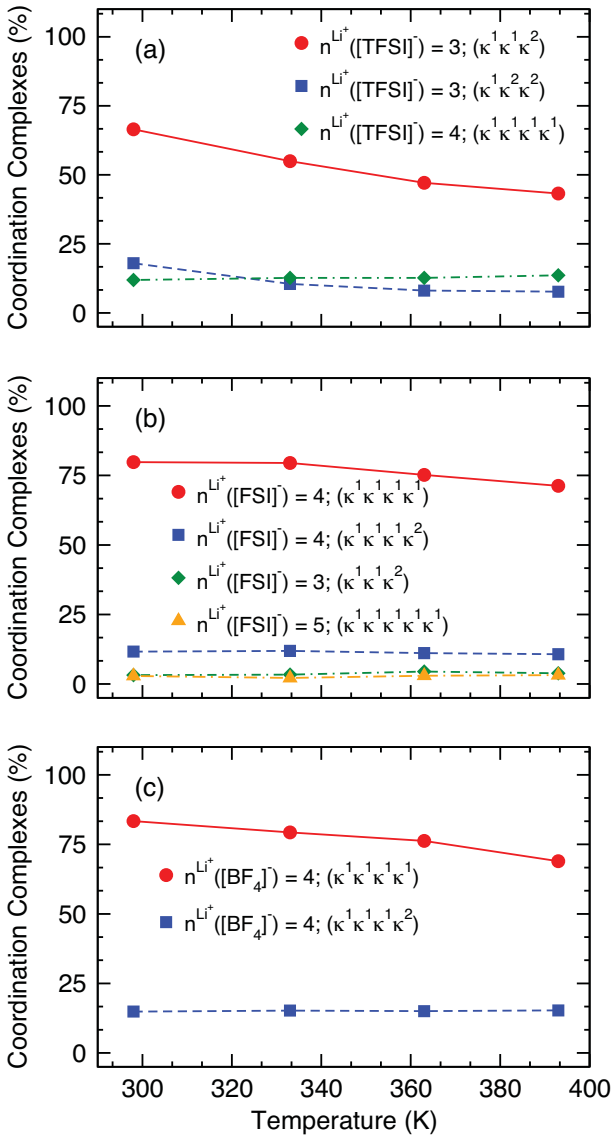

FIGURE S3. Most likely Li^+-anion coordination shells found in (a) [pyr14][TFSI], (b) [pyr13][FSI], and (c) [EMIM][BF_4] for a T range 298 K to 393 K. The values are averaged over simulations at $x_{Li^+} = 0.05$, and the shells are defined by the number of monodentate (κ^1) and bidentate (κ^2) anions in the shell.

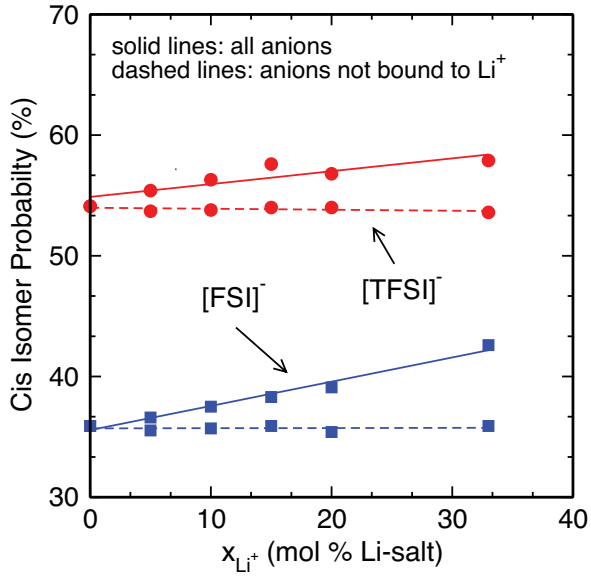

FIGURE S4. Distribution of cis and trans rotamers as a function of Li-salt mole fraction, x_{Li^+}, for anions not bonded with Li^+ (dashed lines) and all anions in the system (solid lines).

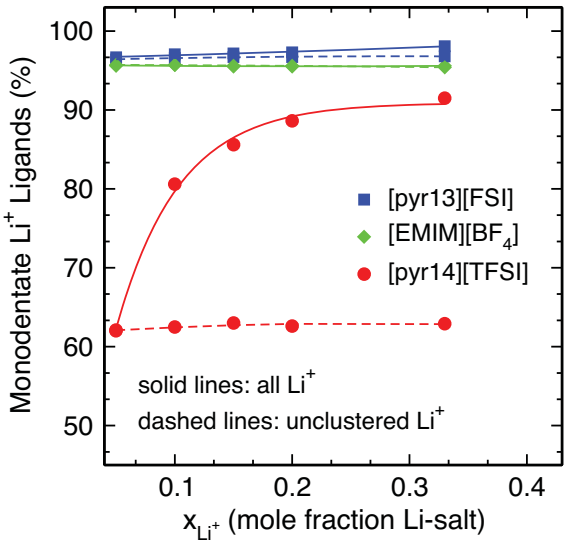

FIGURE S5. Distribution of monodentate bonds to Li^+ as a function of Li-salt mole fraction, x_{Li^+}, for Li ions not associated with a cluster structures (dashed lines) and all Li ions in the system (solid lines).

2. Computational and Experimental Thermodynamics

Measurements for neat [EMIM][BF_4] exhibit a significant hysteresis in conductivity, below -15^{o}C (see Fig. S7). Similar hysteresis has been reported by J. Vila et al. for a number of [EMIM]-based ionic liquids. [1] The observed drop in conductivity occurs well above the solidification temperature tabulated by Galinski for [EMIM][BF_4]. [2] Ionic liquids based on [pyr14][TFSI] were not studied below room temperature in this work.

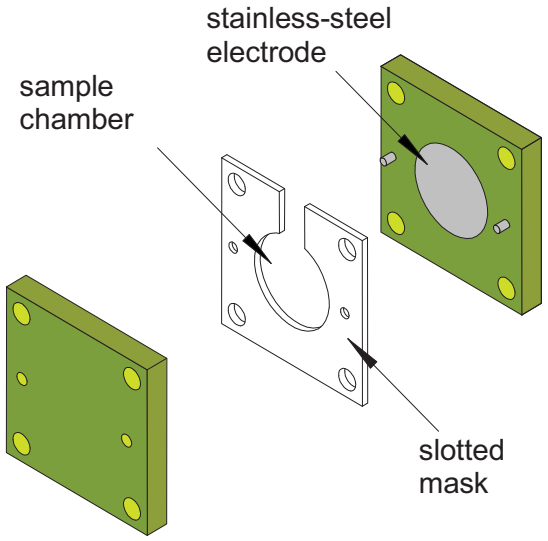

Figure S6. Conductivity fixture.

Table S1. Density and diffusion coefficient of [pyr14][TFSI] and [EMIM][BF_4] at $T = 298$ K for both neat samples and those having 0.5 m Li-salt doping.

	ρ (g/cm^3)	D$^+$ (m^2/s)	D$^-$ (m^2/s)	D^{Li} (m^2/s)
[pyr14][TFSI] (neat)	-	0.1338E-10	0.1029E-10	-
[pyr14][TFSI] (0.5 m Li-salt)	1.44	0.0473E-10	0.0270E-10	0.0248E-10
[EMIM][BF_4] (neat)	-	0.3339E-10	-	-
[EMIM][BF_4] (0.5 m Li-salt)	1.31	0.2329E-10	-	0.0765E-10

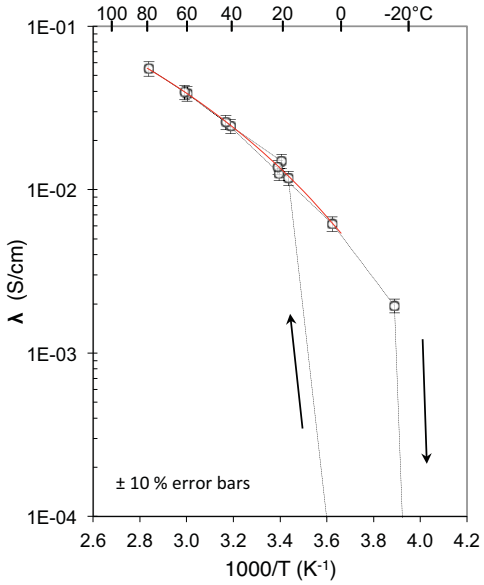

FIGURE S7. Conductivity of neat [EMIM][BF_4].

TABLE S2. T dependence of the ionic conductivity of [pyr14][TFSI] in both the neat form and that having 0.5 m Li-salt doping.

	λ (mS/cm)	
T (K)	[pyr14][TFSI] (neat)	[pyr14][TFSI] (0.5 m Li-salt)
293.0	2.31	1.22
313.0	4.98	2.85
333.0	8.90	5.55
353.0	13.8	8.54

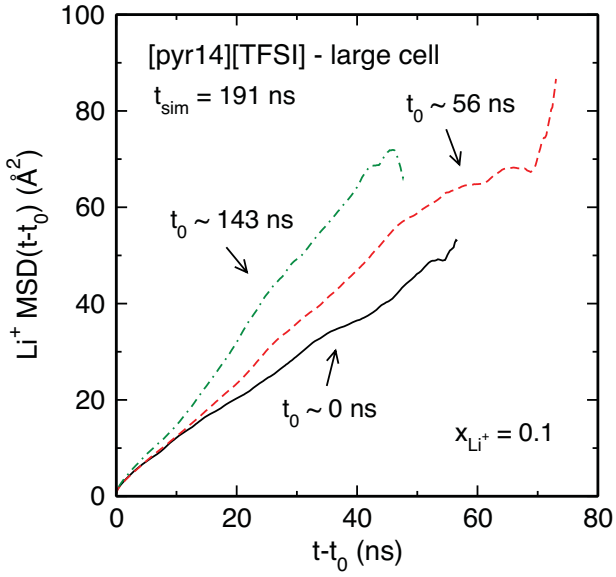

FIGURE S8. Deviation of computed Li^+ MSD as a function of initial state over the course of a 191 ns simulation at $T = 298$ K. The difference between D^{Li^+} taken from the initial trajectory (black solid line) and the final trajectory (green dahed-dotted line) is a factor ~ 2.

TABLE S3. T dependence of the ionic conductivity of [EMIM][BF_4] in both the neat form and that having 0.5 m Li-salt doping.

	λ (mS/cm)	
T (K)	[EMIM][BF_4] (neat)	[EMIM][BF_4] (0.5 m Li-salt)
352.1	63.6	43.6
334.4	47.3	31.1
332.2	43.4	29.7
314.5	29.5	19.3
313.5	28.0	18.4
297.6	17.6	11.0
295.0	16.4	9.7
294.1	15.5	9.6
275.5	7.38	4.0

TABLE S4. T dependence of the ionic conductivity of neat [pyr13][FSI].

T (K)	λ (mS/cm)
253.7	1.4
265.0	2.6
274.6	3.9
277.3	4.4
295.1	8.0
295.2	7.9
296.5	8.3
313.5	13.1
318.1	14.6
333.1	20.0
335.1	20.1
353.1	28.2

TABLE S5. T dependence of the ionic conductivity of a 0.5 m solution of Li[FSI] in [pyr13][FSI].

T (K)	λ (mS/cm)
253.8	0.9
255.3	1.0
264.8	1.7
275.0	2.9
284.1	4.2
293.8	6.0
294.5	6.2
294.8	5.4
307.3	8.6
319.5	12.7
333.5	17.0
339.3	19.4
343.0	20.7
353.0	24.6

References

[1] J. Vila, C. Franjo, J. M. Pico, L. M. Varela, and O. Cabeza. *Port. Electrochim. Acta*, 51:5567–5580, 2006.

[2] M. Galiński, A. Lewandowski, and I. Stępniak. *Electrochim. Acta*, 51:5567–5580, 2006.